

# Variational multiscale residual-based turbulence modeling for large eddy simulation of incompressible flows

Y. Bazilevs<sup>a,\*</sup>, V.M. Calo<sup>a</sup>, J.A. Cottrell<sup>a</sup>, T.J.R. Hughes<sup>a,1</sup>, A. Reali<sup>b</sup>, G. Scovazzi<sup>c,2</sup>

<sup>a</sup> *Institute for Computational Engineering and Sciences, The University of Texas at Austin, 201 East 24th Street,  
1 University Station C0200, Austin, TX 78712, USA*

<sup>b</sup> *Structural Mechanics Department, University of Pavia, via Ferrata 1, 27100 Pavia, Italy*

<sup>c</sup> *1431 Computational Shock and Multi-physics Department, Sandia National Laboratories, P.O. Box 5800, MS 1319, Albuquerque, NM 87185-1319, USA*

Received 2 May 2007; received in revised form 5 July 2007; accepted 19 July 2007

Available online 15 August 2007

## Abstract

We present an LES-type variational multiscale theory of turbulence. Our approach derives **completely from the incompressible Navier–Stokes equations and does not employ any *ad hoc* devices**, such as eddy viscosities. We tested the formulation on forced homogeneous isotropic turbulence and turbulent channel flows. In the calculations, we employed linear, quadratic and cubic NURBS. A dispersion analysis of simple model problems revealed NURBS elements to be superior to classical finite elements in approximating advective and diffusive processes, which play a significant role in turbulence computations. The numerical results are very good and confirm the viability of the theoretical framework.

© 2007 Elsevier B.V. All rights reserved.

**Keywords:** Variational multiscale methods; Large eddy simulation; Turbulence modeling; Optimality; Projection; Small-scale Green's function; Perturbation series; Isogeometric analysis; NURBS; Incompressible flows; Homogeneous isotropic turbulence; Turbulent channel flows

## 1. Introduction

Variational multiscale concepts for Large Eddy Simulation (LES) were introduced in [33]. The basic idea was to use variational projections in place of the traditional filtered equations and to focus modeling on the fine-scale equations. Avoidance of filters eliminates many difficulties associated with the traditional approach, namely, inhomogeneous non-commutative filters necessary for wall-bounded flows, use of complex filtered quantities in compressible flows, etc. In addition, modeling confined to

the fine-scale equations retains numerical consistency in the coarse-scale equations and thus permits full rate-of-convergence of the underlying numerical method in contrast with the usual approach, which limits convergence rate due to artificial viscosity effects in the fully resolved scales ( $O(h^{4/3})$  in the case of Smagorinsky-type models). Initial versions of the variational multiscale method focused on dividing resolved scales into coarse and fine designations, and eddy viscosities, inspired by traditional models, were only included in the fine-scale equations, and acted only on the fine scales. This version was studied in [34,36,56], and found to work very well on homogeneous isotropic flows and fully-developed equilibrium and non-equilibrium turbulent channel flows. Static eddy viscosity models were employed in these studies but superior results were subsequently obtained through the use of dynamic models, as reported in [27,41]. Good numerical results were obtained with the static approach by other investigators, namely, Collis [18], Jeanmart and Winckelmans [44], and

\* Corresponding author.

E-mail address: [bazily@ices.utexas.edu](mailto:bazily@ices.utexas.edu) (Y. Bazilevs).

<sup>1</sup> Aerospace Engineering and Engineering Mechanics, Computational and Applied Mathematics Chair III.

<sup>2</sup> Sandia is a Multiprogram Laboratory Operated by Sandia Corporation, a Lockheed Martin Company, for the United States Department of Energy's National Nuclear Security Administration under Contract DE-AC04-94-AL85000.

Ramakrishnan and Collis [59–62]. Particular mention should be made of the work of Farhat and Koobus [20], and Koobus and Farhat [48], who have implemented this procedure in an unstructured mesh, finite element/finite volume, compressible flow code, and applied it very successfully to a number of complex test cases and industrial flows. A valuable review with many references to relevant literature may be found in [22]. We believe that this initial version of the variational multiscale concept has already demonstrated its viability and practical utility and is, at the very least, competitive with traditional LES turbulence modeling approaches. For a comprehensive treatment of multiscale concepts in turbulence, see [65]. There has also been a number of contributions to the literature in which stabilized numerical methods have been used to model turbulence (see, e.g. [26]). These endeavors are somewhat different in philosophy than the present contribution.

Nevertheless, there is still significant room for improvement. The use of traditional eddy viscosities to represent fine-scale dissipation is an inefficient mechanism. Employing an eddy viscosity in the resolved fine scales to represent turbulent dissipation introduces a consistency error, which results in the resolved fine scales being sacrificed to retain full consistency in the coarse scales. (In our opinion, this is still better than the traditional approach in which consistency in all resolved scales is sacrificed to represent turbulent dissipation.) This procedure is felt to be inefficient because approximately 7/8 of the resolved scales are typically ascribed to the fine scales. Another shortcoming noted for the initial version of the variational multiscale method is too small an energy transfer to unresolved modes when the discretization is very coarse (see, e.g. [41]). This phenomenon is also noted for some traditional models, such as the dynamic Smagorinsky model, Hughes et al. [41], but, by design, is more pronounced for the multiscale version of the dynamic model. *The objectives of recent multiscale work have been to capture all scales consistently and to avoid use of eddy viscosities altogether.* This holds the promise of much more accurate and efficient LES procedures. In this work, we describe a new variational multiscale formulation, which makes considerable progress toward these goals. In what follows, all resolved scales are viewed as coarse scales, which obviates the aforementioned issue of inefficiency *ab initio*.

We begin by taking the view that the decomposition into coarse and fine scales is exact. For example, in the spectral case, the coarse-scale space consists of all Fourier modes beneath some cut-off wave number and the fine-scale space consists of all remaining Fourier modes. Consequently, the coarse-scale space has finite dimension whereas the fine-scale space is infinite dimensional. The derivation of the coarse- and fine-scale equations proceeds, first, by substituting the split of the exact solution into coarse and fine scales into the Navier–Stokes equations, then, second, by projecting this equation into the coarse- and fine-scale subspaces. The projection into coarse scales is a finite-dimensional system for the coarse-scale component of the

solution, which depends parametrically on the fine-scale component. In the spectral case, in addition to the usual terms involving the coarse-scale component, only the cross-stress and Reynolds-stress terms involve the fine-scale component. In the case of non-orthogonal bases, even the linear terms give rise to coupling between coarse and fine scales. The coarse-scale component plays an analogous role to the filtered field in the classical approach, but has the advantage of avoiding all problems associated with homogeneity, commutativity, walls, compressibility, etc. The projection into fine scales is an infinite-dimensional system for the fine-scale component of the solution, which depends parametrically on the coarse-scale component. We also assume the cut-off wave number is sufficiently large that the philosophy of LES is appropriate. For example, if there is a well-defined inertial sub-range, then we assume the cut-off wave number resides somewhere within it. This assumption enables us to further assume that the energy content in the fine scales is small compared with the coarse scales. This turns out to be important in our efforts to analytically represent the solution of the fine-scale equations. The strategy is to obtain approximate analytical expressions for the fine scales then substitute them into the coarse-scale equations which are, in turn, solved numerically. If the scale decomposition is performed in space and time, the *only* approximation in the procedure is the representation of the fine-scale solution. To provide a framework for the fine-scale approximation, we assume an infinite perturbation series expansion to treat the fine-scale nonlinear term in the fine-scale equation. By virtue of the smallness of the fine scales, this expansion is expected to converge rapidly under the circumstances described in many cases of practical interest. The remaining part of the fine-scale Navier–Stokes system is the *linearized* operator which is formally inverted through the use of a matrix Green’s function. The combination of a perturbation series and Green’s function provides an exact formal solution of the fine-scale Navier–Stokes equations. The driving force in these equations is the Navier–Stokes system residual computed from the coarse scales. This expresses the intuitively obvious fact that if the coarse scales constitute a good approximation to the solution of the problem, the coarse-scale residual will be small and the resulting fine-scale solution will be small as well. This is the case we have in mind and it provides a rational basis for assuming the perturbation series converges rapidly. Note that one cannot use such an argument on the original problem because in this case the perturbation series would almost definitely fail to converge. (If we could have used this argument, we would have solved the Navier–Stokes equations analytically! Unfortunately, it does not work.) The formal solution of the fine-scale equations suggests various approximations may be employed in practical problem solving. We are tempted to use the word “modeling” because approximate analytical representations of the fine scales constitute the only approximation and hence may be thought of as the “modeling” component of the present approach but we want to emphasize

that it is very different from classical modeling ideas which are dominated by the *addition* of *ad hoc* eddy viscosities. We will present numerical results that demonstrate these eddy viscosity terms are unnecessary in the present circumstances. There are two aspects to the approximation of the fine scales: (1) approximation of the matrix Green's function for the linearized Navier–Stokes system and (2) approximation of the nonlinearities represented by the perturbation series. The first and obvious thought for the latter aspect, nonlinearity, is to simply truncate the perturbation series. This idea is investigated, as well as another promising idea, in conjunction with some simple approximations of the Green's function. It turns out there is considerable experience in local scaling approximations of the Green's function based on the theory of stabilized methods [28,31,39]. These ideas derive inspiration from the asymptotic approaches of Barenblatt [2]. The Green's function is typically approximated by locally defined algebraic operators (i.e., the “ $\tau$ 's” of stabilized methods) multiplied by local values of the coarse-scale residual. With this approximation of the solution of the linearized operator, nonlinearities can be easily accounted for in perturbation series fashion.

The remainder of the paper is summarized as follows: In Section 2 we present the mathematical details of the variational multiscale theory described previously. This represents our general approach to LES-style turbulence modeling and is independent of the specifics of the discrete spaces utilized to represent the coarse scales. In Section 3, we present ideas supporting the use of simplified scaling arguments to represent the fine scales. In Section 4, we describe the implementational aspects of the procedures used herein and the details of the fine-scale approximation. The relationship between this version of the variational multiscale method and classical stabilized methods is delineated. The variational multiscale method includes additional terms. Both conceptually and from the point of view of actual implementation, stabilized methods may be viewed as historical stepping stones leading to the more coherent variational multiscale formulation. In Section 5, the time integration techniques are presented. In Section 6, we present our numerical studies of forced isotropic turbulence at  $Re_\lambda = 165$  and  $Re_\lambda = \infty$ . ( $Re_\lambda$  is the Taylor microscale Reynolds number.) We begin in Section 6.1 with a description of the approximation spaces consisting of NURBS elements (non-uniform rational B-splines, see, e.g. [63,57,21,17]). In the case of the rectilinear geometry considered, NURBS reduce to B-splines, which have been advocated for turbulence calculations previously (see [49,68,50,51]). We employ trivariate linear, quadratic, and cubic NURBS with periodic boundary conditions. Linear trivariate NURBS turn out to be identical to trilinear hexahedral finite elements, but the higher-order NURBS are different than classical higher-order finite elements. In Section 6.2, we perform a dispersion error analysis for NURBS versus classical finite elements on simple, linear, one-dimensional advective and diffusive model problems, and conclude that NURBS have better

approximation properties than classical finite elements. In Section 6.3, we describe the way we force the turbulence and in Section 6.4 we present the results of our numerical calculations. We employ meshes of  $32^3$ ,  $64^3$ ,  $128^3$ , and  $256^3$  to explore convergence with mesh refinement ( $h$ -convergence) and we examine the behavior of increasing order from linear to cubic on fixed meshes ( $k$ -convergence). In the case of  $Re_\lambda = 165$ , we compare with the DNS spectral results of Langford and Moser [52]. Energy spectra and third-order structure functions are presented. Our assessment is that the results are very good for all cases. In the case of  $Re_\lambda = \infty$  we can clearly see the development of an inertial subrange. In Section 7 we present results for turbulent channel flows at  $Re_\tau = 395$ . ( $Re_\tau$  is the wall-friction Reynolds number.) We employ meshes of  $32^3$  and  $64^3$ . This time the mesh is graded in the wall-normal direction to better capture the boundary layer. Again, we consider convergence from the  $h$ - and  $k$ -refinement perspectives. A striking result is how much better quadratic elements are than linear elements. For a mesh of  $64^3$ , the quadratic and cubic results are essentially identical to the DNS results of Moser et al. [55] for first- and second-order statistics, and for a mesh of  $32^3$  they are in close agreement. Conclusions are drawn in Section 8.

## 2. Variational multiscale formulation of the incompressible Navier–Stokes equations

In this section we describe our turbulence modeling theory.

### 2.1. Incompressible Navier–Stokes equations

We consider a space-time domain  $Q = \Omega \times ]0, T[ \subset \mathbb{R}^3 \times \mathbb{R}^+$  with lateral boundary  $P = \Gamma \times ]0, T[$ , as illustrated in the left-hand side of Fig. 1. The initial/boundary-value problem consists of solving the following equations for  $\mathbf{u} : \overline{Q} \rightarrow \mathbb{R}^3$ , the velocity, and  $p : Q \rightarrow \mathbb{R}$ , the pressure (divided by the constant density),

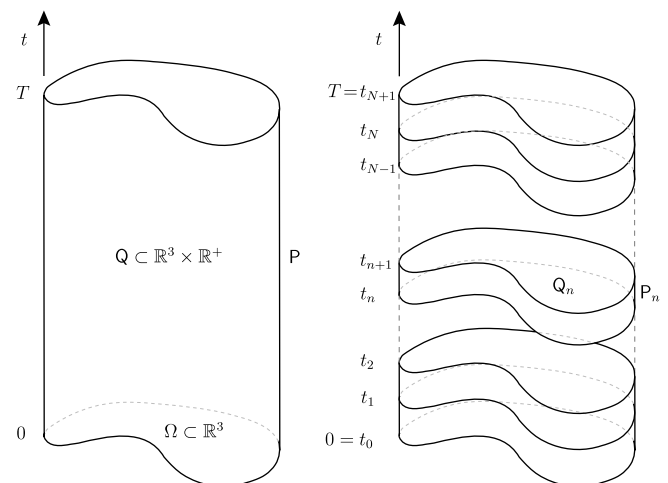


Fig. 1. Space-time domain (left) and slicing into space-time slabs (right).

$$\frac{\partial \mathbf{u}}{\partial t} + \nabla \cdot (\mathbf{u} \otimes \mathbf{u}) + \nabla p = \nu \Delta \mathbf{u} + \mathbf{f} \quad \text{in } Q, \quad (1)$$

$$\nabla \cdot \mathbf{u} = 0 \quad \text{in } Q, \quad (2)$$

$$\mathbf{u} = \mathbf{0} \quad \text{on } P, \quad (3)$$

$$\mathbf{u}(0^+) = \mathbf{u}(0^-) \quad \text{on } \Omega, \quad (4)$$

where  $\mathbf{f} : Q \rightarrow \mathbb{R}^d$  is the given body force (per unit volume);  $\nu$  is the kinematic viscosity, assumed positive and constant;  $\mathbf{u}(0^-) : \Omega \rightarrow \mathbb{R}^d$  is the given initial velocity; and  $\otimes$  denotes the tensor product (e.g., in component notation,  $[\mathbf{u} \otimes \mathbf{v}]_{ij} = u_i v_j$ ).

Eqs. (1)–(4) are, respectively, the linear momentum balance, the incompressibility constraint, the no-slip boundary condition and the initial condition.

### 2.1.1. Global space-time variational formulation

Let  $\mathcal{V} = \mathcal{V}(Q)$  denote both the trial solution and weighting function spaces, which are assumed to be identical. We assume  $\mathbf{U} = \{\mathbf{u}, p\} \in \mathcal{V}$  implies  $\mathbf{u} = \mathbf{0}$  on  $P$  and  $\int_{\Omega} p(t) d\Omega = 0$  for all  $t \in ]0, T[$ . Let  $(\cdot, \cdot)_{\omega}$  denote the  $L^2$  inner product with respect to the domain  $\omega$ . The variational formulation is stated as follows:

Find  $\mathbf{U} \in \mathcal{V}$  such that  $\forall \mathbf{W} = \{\mathbf{w}, q\} \in \mathcal{V}$ :

$$B(\mathbf{W}, \mathbf{U}) = B_1(\mathbf{W}, \mathbf{U}) + B_2(\mathbf{W}, \mathbf{U}, \mathbf{U}) = L(\mathbf{W}) \quad (5)$$

with

$$B_1(\mathbf{W}, \mathbf{U}) = (\mathbf{w}(T^-), \mathbf{u}(T^-))_{\Omega} - \left( \frac{\partial \mathbf{w}}{\partial t}, \mathbf{u} \right)_{\Omega} + (q, \nabla \cdot \mathbf{u})_{\Omega} - (\nabla \cdot \mathbf{w}, p)_{\Omega} + (\nabla^s \mathbf{w}, 2\nu \nabla^s \mathbf{u})_{\Omega}, \quad (6)$$

$$B_2(\mathbf{W}, \mathbf{U}, \mathbf{V}) = -(\nabla \mathbf{w}, \mathbf{u} \otimes \mathbf{v})_{\Omega}, \quad (7)$$

$$L(\mathbf{W}) = (\mathbf{w}, \mathbf{f})_{\Omega} + (\mathbf{w}(0^+), \mathbf{u}(0^-))_{\Omega}, \quad (8)$$

where  $\mathbf{V} = \{\mathbf{v}, \cdot\}$  and  $\nabla^s \mathbf{u} = (\nabla \mathbf{u} + (\nabla \mathbf{u})^T)/2$ . Note that  $B_1(\cdot, \cdot)$  is a bilinear form and  $B_2(\cdot, \cdot, \cdot)$  is a trilinear form. Assuming sufficient regularity and integrating by parts, we obtain the Euler–Lagrange form of (5)–(8):

$$0 = \left( \mathbf{w}, \frac{\partial \mathbf{u}}{\partial t} + \nabla \cdot (\mathbf{u} \otimes \mathbf{u}) + \nabla p - \nabla \cdot 2\nu \nabla^s \mathbf{u} - \mathbf{f} \right)_{\Omega} + (q, \nabla \cdot \mathbf{u})_{\Omega} + (\mathbf{w}(0^+), \mathbf{u}(0^+) - \mathbf{u}(0^-))_{\Omega} \quad (9)$$

which reveals that the variational formulation implies satisfaction of the momentum equations, incompressibility constraint, and initial condition. The velocity boundary condition is built into the definition of the space  $\mathcal{V}$ . In summary, the variational formulation is equivalent to (1)–(4).

### 2.1.2. Sliced space-time variational formulation

Consider a *slicing* of space-time obtained by replacing  $]0, T[$  by  $]t_n, t_{n+1}[$ ,  $n = 0, 1, 2, \dots, N$ , and summing over the space-time *slabs*  $Q_n$  (see Fig. 1). The counterparts of (5)–(9) for a typical slab are:

$$B(\mathbf{W}, \mathbf{U})_n = B_1(\mathbf{W}, \mathbf{U})_n + B_2(\mathbf{W}, \mathbf{U}, \mathbf{U})_n = L(\mathbf{W})_n, \quad (10)$$

$$B_1(\mathbf{W}, \mathbf{U})_n = (\mathbf{w}(t_{n+1}^-), \mathbf{u}(t_{n+1}^-))_{\Omega} - \left( \frac{\partial \mathbf{w}}{\partial t}, \mathbf{u} \right)_{Q_n} + (q, \nabla \cdot \mathbf{u})_{Q_n} - (\nabla \cdot \mathbf{w}, p)_{Q_n} + (\nabla^s \mathbf{w}, 2\nu \nabla^s \mathbf{u})_{Q_n}, \quad (11)$$

$$B_2(\mathbf{W}, \mathbf{U}, \mathbf{V})_n = -(\nabla \mathbf{w}, \mathbf{u} \otimes \mathbf{v})_{Q_n}, \quad (12)$$

$$L(\mathbf{W})_n = (\mathbf{w}, \mathbf{f})_{Q_n} + (\mathbf{w}(t_n^+), \mathbf{u}(t_n^-))_{\Omega}, \quad (13)$$

$$0 = \left( \mathbf{w}, \frac{\partial \mathbf{u}}{\partial t} + \nabla \cdot (\mathbf{u} \otimes \mathbf{u}) + \nabla p - \nabla \cdot 2\nu \nabla^s \mathbf{u} - \mathbf{f} \right)_{Q_n} + (q, \nabla \cdot \mathbf{u})_{Q_n} + (\mathbf{w}(t_n^+), \mathbf{u}(t_n^+) - \mathbf{u}(t_n^-))_{\Omega}, \quad (14)$$

where in (10)–(14),  $\mathbf{U} = \{\mathbf{u}, p\}$  and  $\mathbf{W} = \{\mathbf{w}, q\}$  belong to  $\mathcal{V}_n = \mathcal{V}(Q_n)$ , the restriction of  $\mathcal{V}$  to  $Q_n$ . From the Euler–Lagrange form of the equation, (14), we see that the momentum equation and incompressibility constraint are satisfied on the slab, and the solution is continuous across slab interfaces. The formulation in terms of space-time slabs exploits the causal nature of the Navier–Stokes equations and reduces the overall problem to a succession of initial/boundary-value problems on the slabs. The solution is obtained solving the variational equation on each slab successively,  $n = 0, 1, 2, \dots, N$ . We emphasize that this is an *exact* formulation, entirely equivalent to (5)–(9), and (1)–(4). However, it is a more suitable starting point for the development of numerical schemes.

#### Remark

In order to simplify notation in the sequel, we will work with the global form of the variational equation. However, all results are equally applicable to the variational equations of the individual space-time slabs.

### 2.2. Scale separation

We consider a direct-sum decomposition of  $\mathcal{V}$  into “coarse-scale” and “fine-scale” subspaces,  $\overline{\mathcal{V}}$  and  $\mathcal{V}'$ , respectively,

$$\mathcal{V} = \overline{\mathcal{V}} \oplus \mathcal{V}'. \quad (15)$$

$\overline{\mathcal{V}}$  is assumed to be a finite-dimensional space and it will be identified later with the space of functions with which we actually compute. In order to make the decomposition well defined, we need to introduce a procedure for uniquely determining  $\overline{\mathbf{U}} \in \overline{\mathcal{V}}$  and  $\mathbf{U}' \in \mathcal{V}'$  from a given  $\mathbf{U} \in \mathcal{V}$ . This can be accomplished with the aid of a projector  $\overline{\mathbb{P}} : \mathcal{V} \rightarrow \overline{\mathcal{V}}$ . For example,  $\overline{\mathbb{P}}$  could be the  $L^2$ -projector,  $H^1$ -projector, etc. There are infinitely many possibilities.<sup>3</sup>

<sup>3</sup> The way  $\overline{\mathbf{U}}$  is determined from  $\mathbf{U}$  is a very important issue, and it has very significant impact on the theory to be developed. An initiatory study of typical projectors is presented in [37]. Not only can one envision an infinite number of possible projectors, but one can also envision an infinite number of nonlinear optimization schemes that “fit”  $\overline{\mathbf{U}}$  to  $\mathbf{U}$ . In some applications nonlinear schemes will surely be important, an example being compressible turbulence with shocks where monotonicity is important. However, for incompressible turbulence, we feel linear projectors, such as the  $H^1$ -projector, should suffice. (See [35] for an application of the  $H^1$ -projector in turbulence.)



Once  $\overline{\mathbb{P}}$  is selected, we know how the coarse scales approximate all scales, viz.,

$$\overline{U} = \overline{\mathbb{P}}U, \quad (16)$$

$$U' = U - \overline{\mathbb{P}}U = (\mathbb{I} - \overline{\mathbb{P}})U, \quad (17)$$

where  $\mathbb{I}$  is the identity operator. Likewise, we can decompose a weighting function into its coarse- and fine-scale components:

$$\overline{W} = \overline{\mathbb{P}}W, \quad (18)$$

$$W' = W - \overline{\mathbb{P}}W = (\mathbb{I} - \overline{\mathbb{P}})W. \quad (19)$$

With these, we may decompose the original variational equation into coupled coarse-scale and fine-scale equations, viz.,

$$B(\overline{W}, \overline{U} + U') = L(\overline{W}), \quad (20)$$

$$B(W', \overline{U} + U') = L(W'), \quad (21)$$

where

$$\begin{aligned} B(\overline{W}, \overline{U} + U') &= B_1(\overline{W}, \overline{U}) + B_1(\overline{W}, U') \\ &\quad + B_2(\overline{W}, \overline{U}, \overline{U}) + B_2(\overline{W}, \overline{U}, U') \\ &\quad + B_2(\overline{W}, U', \overline{U}) + B_2(\overline{W}, U', U'), \end{aligned} \quad (22)$$

$$\begin{aligned} B(W', \overline{U} + U') &= B_1(W', \overline{U}) + B_1(W', U') \\ &\quad + B_2(W', \overline{U}, \overline{U}) + B_2(W', \overline{U}, U') \\ &\quad + B_2(W', U', \overline{U}) + B_2(W', U', U'). \end{aligned} \quad (23)$$

In (22),  $B_2(\overline{W}, \overline{U}, U')$  and  $B_2(\overline{W}, U', \overline{U})$  correspond to the cross-stress terms, and  $B_2(\overline{W}, U', U')$  corresponds to the Reynolds stress term. Eq. (21) can be expressed as

$$B_{\overline{U}}(W', U') + B_2(W', U', U') = \langle W', \text{Res}(\overline{U}) \rangle_{\mathcal{V}', \mathcal{V}'^*}, \quad (24)$$

where

$$B_{\overline{U}}(W', U') = B_1(W', U') + B_2(W', U', \overline{U}) + B_2(W', \overline{U}, U') \quad (25)$$

$$\langle W', \text{Res}(\overline{U}) \rangle_{\mathcal{V}', \mathcal{V}'^*} = L(W') - B_1(W', \overline{U}) - B_2(W', \overline{U}, \overline{U}) \quad (26)$$

in which  $\text{Res}(\overline{U})$  is the coarse-scale residual “lifted” to the dual of the fine-scale space  $\mathcal{V}'^*$ ,  $\langle \cdot, \cdot \rangle_{\mathcal{V}', \mathcal{V}'^*}$  is the duality pairing, and

$$B_{\overline{U}}(\cdot, U') = \left( \frac{d}{d\varepsilon} B(\cdot, \overline{U} + \varepsilon U') \right)_{\varepsilon=0} \quad (27)$$

the linearization of  $B(\cdot, \overline{U} + U')$  about  $\overline{U}$  in the direction  $U'$ . Note that the solution of (24) can be formally represented as a functional of  $\overline{U}$  and  $\text{Res}(\overline{U})$ , namely,

$$\boxed{U' = F'(\overline{U}, \text{Res}(\overline{U}))} \quad (28)$$

The explicit dependence on  $\overline{U}$  in the first argument of  $F'$  emanates from the dependence of the linearized operator  $B_{\overline{U}}$  on  $\overline{U}$ . This expression can be inserted into (20) to “close” the finite-dimensional system for  $\overline{U}$ ,

$$\boxed{B(\overline{W}, \overline{U} + F'(\overline{U}, \text{Res}(\overline{U}))) = L(\overline{W})} \quad (29)$$

Eqs. (28) and (29) can be thought of in global terms or in terms of a sequence of space-time slabs. In both cases, they represent a procedure for solving the Navier–Stokes equations in terms of a scale decomposition of the solution. So far we have not discussed approximations or numerics. The solution  $U = \overline{U} + U'$ , where  $\overline{U}$  is determined by solving (29) and  $U'$  is determined from  $\overline{U}$  through (28), is the *exact* solution of the original variational problem, (20) and (21), and (1)–(4), the Navier–Stokes initial/boundary-value problem.

Our plan for turbulence modeling is to systematically *approximate* the functional  $F'$ . This will provide us with a parameterization of the fine scales in terms of the coarse scales, which can be substituted in the coarse-scale equation, “closing” it. The finite-dimensional coarse-scale equation can then be solved. In this way we obtain an approximate coarse-scale solution and an estimation of the fine scales. In summary, our variational multiscale theory of turbulence modeling is encapsulated in the following equations:

$$\boxed{\tilde{U}' = \tilde{F}'(\tilde{U}, \text{Res}(\tilde{U}))} \quad (30)$$

$$\boxed{B(\overline{W}, \tilde{U} + \tilde{F}'(\tilde{U}, \text{Res}(\tilde{U}))) = L(\overline{W})} \quad (31)$$

where  $\tilde{F}'$  is an approximation of the exact functional  $F'$ , and  $\tilde{U}'$  and  $\tilde{U}$  are the approximations of  $U'$  and  $\overline{U}$ , respectively. The concept underlying the model is illustrated in Fig. 2. We also note that (30) constitutes an *a posteriori* estimation of the *error* in the coarse-scale solution (see [31,39,24,25]).

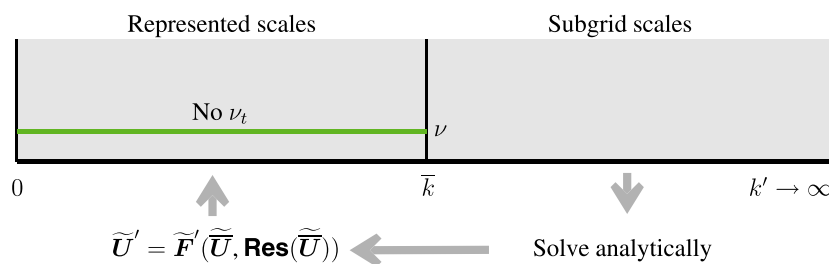


Fig. 2. The variational multiscale turbulence modeling theory is schematically illustrated. The fine, or “subgrid” scales are solved for analytically and substituted into the coarse-scale equation. The coarse scales are the represented scales in a calculation. Note that there is no *ad hoc* eddy viscosity model introduced.

### Remarks

- (1) (31) may be thought of as playing a similar role in the variational multiscale theory as the filtered equations play in traditional turbulence modeling. Distinguishing features are (31) is finite-dimensional and closed, in contrast with the filtered equations.
- (2) Intuitively, the “better” the fine-scale approximation, the smaller the dimension of the coarse-scale space required, and consequently, the smaller the computational effort. It is also possible to envision a hierarchy of approximations that produce variational multiscale analogues of traditional turbulence modeling concepts, such as large eddy simulation (LES), detached eddy simulation (DES), and the Reynolds averaged Navier–Stokes (RANS) approach. LES represents the turbulence modeling methodology requiring the greatest computational burden, but perhaps the least complex modeling. In the following sections we will endeavor to develop a variational multiscale analogue of LES within the theoretical framework of (30) and (31).
- (3) It is very important to emphasize that in practice we work directly with (31), a finite-dimensional system, and we consider the solution of (31),  $\bar{U}$ , our approximation to  $\bar{U}$ , and in turn our approximation to  $U$ . Recall, by design of  $\mathbb{P}$ ,  $\bar{U}$  is an approximation to  $U$ . We do not need to solve for the fine scales and because of this (30) is completely extraneous, unless we wish to use it to estimate the error in the coarse scales. That being said, it may also be interesting to consider  $\bar{U} + \bar{U}'$  as an alternative approximation to  $U$ . It will of course be necessary to assume that the coarse-scale space is sufficiently large for the philosophy of LES to be appropriate. That is, if there is a well-defined inertial subrange, then we assume the cut-off between the coarse- and fine-scale spaces resides somewhere within it. This assumption enables us to further assume that the energy content in the fine scales is small compared with the coarse scales, an aspect of considerable importance in attempting to analytically determine the solution of the fine-scale equations.

### 2.3. Perturbation series

It seems reasonable to assume that the larger the space  $\bar{\mathcal{V}}$ , the better the approximation of  $\bar{U}$  to  $U$ , and the smaller the coarse-scale residual  $\mathbf{Res}(\bar{U}) \in \mathcal{V}'^*$ . We further assume that if  $\mathbf{Res}(\bar{U}) = \mathbf{0}$ , then  $\mathbf{F}'(\bar{U}, \mathbf{0}) = \mathbf{0}$ , and if  $\mathbf{Res}(\bar{U})$  is “small”, then  $\bar{U}'$  will likewise be “small”.<sup>4</sup> These assumptions suggest a perturbation series expansion of the form:

$$\bar{U}' = \varepsilon \bar{U}'_1 + \varepsilon^2 \bar{U}'_2 + \varepsilon^3 \bar{U}'_3 + \cdots = \sum_{k=1}^{\infty} \varepsilon^k \bar{U}'_k, \quad (32)$$

where  $\varepsilon = \|\mathbf{Res}(\bar{U})\|_{\mathcal{V}'^*}$ . Let us rewrite (24) in terms of the proposed expansion:

$$B_{\bar{U}}\left(\bar{W}', \sum_{k=1}^{\infty} \varepsilon^k \bar{U}'_k\right) + B_2\left(\bar{W}', \sum_{k=1}^{\infty} \varepsilon^k \bar{U}'_k, \sum_{k=1}^{\infty} \varepsilon^k \bar{U}'_k\right) = \varepsilon \langle \bar{W}', \hat{\mathbf{R}}(\bar{U}) \rangle \quad (33)$$

where  $\langle \cdot, \cdot \rangle = \langle \cdot, \cdot \rangle_{\mathcal{V}', \mathcal{V}'^*}$ , and

$$\hat{\mathbf{R}}(\bar{U}) = \frac{\mathbf{Res}(\bar{U})}{\|\mathbf{Res}(\bar{U})\|_{\mathcal{V}'^*}}. \quad (34)$$

Notice that, by linearity,

$$B_{\bar{U}}\left(\bar{W}', \sum_{k=1}^{\infty} \varepsilon^k \bar{U}'_k\right) = \sum_{k=1}^{\infty} \varepsilon^k B_{\bar{U}}(\bar{W}', \bar{U}'_k), \quad (35)$$

while the second term requires further consideration. We expand it as follows:

$$\begin{aligned} B_2(\bar{W}', \varepsilon \bar{U}'_1 + \varepsilon^2 \bar{U}'_2 + \varepsilon^3 \bar{U}'_3 + \cdots, \varepsilon \bar{U}'_1 + \varepsilon^2 \bar{U}'_2 + \varepsilon^3 \bar{U}'_3 + \cdots) \\ = \varepsilon^2 B_2(\bar{W}', \bar{U}'_1, \bar{U}'_1) + \varepsilon^3 [B_2(\bar{W}', \bar{U}'_1, \bar{U}'_2) \\ + B_2(\bar{W}', \bar{U}'_2, \bar{U}'_1)] + \varepsilon^4 [B_2(\bar{W}', \bar{U}'_1, \bar{U}'_3) \\ + B_2(\bar{W}', \bar{U}'_2, \bar{U}'_2) + B_2(\bar{W}', \bar{U}'_3, \bar{U}'_1)] + \cdots \end{aligned} \quad (36)$$

A recurrence formula can be easily deduced, by grouping coefficients of the powers of  $\varepsilon$ :

$$\begin{aligned} \varepsilon^2 &\rightarrow B_2(\bar{W}', \bar{U}'_1, \bar{U}'_1), \\ \varepsilon^3 &\rightarrow B_2(\bar{W}', \bar{U}'_1, \bar{U}'_2) + B_2(\bar{W}', \bar{U}'_2, \bar{U}'_1), \\ \varepsilon^4 &\rightarrow B_2(\bar{W}', \bar{U}'_1, \bar{U}'_3) + B_2(\bar{W}', \bar{U}'_2, \bar{U}'_2) + B_2(\bar{W}', \bar{U}'_3, \bar{U}'_1), \\ \varepsilon^5 &\rightarrow \cdots + \cdots + \cdots + \cdots \end{aligned}$$

Hence

$$B_2\left(\bar{W}', \sum_{k=1}^{\infty} \varepsilon^k \bar{U}'_k, \sum_{k=1}^{\infty} \varepsilon^k \bar{U}'_k\right) = \sum_{k=2}^{\infty} \varepsilon^k \sum_{j=1}^{k-1} B_2(\bar{W}', \bar{U}'_j, \bar{U}'_{k-j}). \quad (37)$$

The full expansion of the equation can be compactly written as

$$\begin{aligned} \sum_{k=1}^{\infty} \varepsilon^k B_{\bar{U}}(\bar{W}', \bar{U}'_k) + \sum_{k=2}^{\infty} \varepsilon^k \sum_{j=1}^{k-1} B_2(\bar{W}', \bar{U}'_j, \bar{U}'_{k-j}) \\ = \varepsilon \langle \bar{W}', \hat{\mathbf{R}}(\bar{U}) \rangle. \end{aligned} \quad (38)$$

Equating like coefficients, we obtain a sequence of linear variational problems coupled through their right-hand sides:

$$\text{For } k = 1 \quad B_{\bar{U}}(\bar{W}', \bar{U}'_1) = \langle \bar{W}', \hat{\mathbf{R}}(\bar{U}) \rangle_{\mathcal{V}', \mathcal{V}'^*}, \quad (39)$$

$$\text{For } k \geq 2 \quad B_{\bar{U}}(\bar{W}', \bar{U}'_k) = - \sum_{j=1}^{k-1} B_2(\bar{W}', \bar{U}'_j, \bar{U}'_{k-j}). \quad (40)$$

<sup>4</sup> These assumptions seem physically reasonable, but rigorous mathematical justification may be difficult to obtain. The existence of non-trivial, unforced weak solutions of the Euler equations, compact in space and time, underscores the mathematical difficulties of the Navier–Stokes equations at large Reynolds numbers (see [69]).

The bilinear operator  $B_{\overline{U}}(\cdot, \cdot)$  is the same for all the problems in the cascade, and can be formally inverted through a Green's operator. The Green's operator concept can be introduced in an abstract sense through a *resolvent* operator:

$$\mathbf{G}'_{\overline{U}}(\cdot) = \mathbf{G}'(\overline{U}, \cdot) : \mathcal{V}'^{ts} \rightarrow \mathcal{V}', \quad (41)$$

$$\mathcal{F}(\cdot) \mapsto \mathbf{V}'. \quad (42)$$

such that

$$B_{\overline{U}}(\mathbf{W}', \mathbf{V}') = \mathcal{F}(\mathbf{W}'). \quad (43)$$

If a sequence of operators  $\mathcal{F}_j : \mathcal{V}' \rightarrow \mathbb{R}$  (i.e.,  $\mathcal{F}_j \in \mathcal{V}'^{ts}$ ) is defined as

$$\begin{aligned} \text{For } k = 1 \quad \mathcal{F}_1(\mathbf{W}') &= \mathcal{F}_1(\mathbf{W}'; \widehat{\mathbf{R}}(\overline{U})) \\ &= \langle \mathbf{W}', \widehat{\mathbf{R}}(\overline{U}) \rangle_{\mathcal{V}', \mathcal{V}'^{ts}}, \end{aligned} \quad (44)$$

$$\begin{aligned} \text{For } k \geq 2 \quad \mathcal{F}_k(\mathbf{W}') &= \mathcal{F}_k(\mathbf{W}'; \mathbf{U}'_1, \dots, \mathbf{U}'_{k-1}) \\ &= - \sum_{j=1}^{k-1} B_2(\mathbf{W}', \mathbf{U}'_j, \mathbf{U}'_{k-j}) \end{aligned} \quad (45)$$

then it is possible to reformulate the sequence of problems (39) and (40) as

$$\mathbf{U}'_k = \mathbf{G}'_{\overline{U}}(\mathcal{F}_k) = \mathbf{G}'(\overline{U}, \mathcal{F}_k), \quad k = 1, 2, \dots \quad (46)$$

Notice that in the cascade of problems (39) and (40) (or, equivalently, (44) and (45), or (46)) the level- $k$  term in the expansion depends on terms on the right-hand side, which involve the coarse-scale residual and terms in the expansion from level 1 to  $k-1$ .

Upon substituting the  $\mathbf{U}'_k$ 's into the series (32), the powers of  $\varepsilon = \|\mathbf{Res}(\overline{U})\|_{\mathcal{V}'^{ts}}$  cancel out. If the series converges, it represents an exact solution to the fine-scale equation, and then (31) gives the exact solution of the coarse-scale equation. In other words, given the validity of the assumptions, the exact solution of the original Navier–Stokes system is obtained. In order to determine the exact solutions of each of the linear problems in the cascade, we need the exact Green's operator  $\mathbf{G}'_{\overline{U}}$ . This is a *non-classical* Green's operator, referred to as the “fine-scale Green's operator,” that in turn depends on the *classical* Green's operator and the selected projector  $\overline{\mathbb{P}}$  (see [37]):

$$\mathbf{G}' = \mathbf{G} - \mathbf{G}\overline{\mathbb{P}}^*(\overline{\mathbb{P}}\mathbf{G}\overline{\mathbb{P}}^*)^{-1}\overline{\mathbb{P}}\mathbf{G}, \quad (47)$$

where  $\overline{\mathbb{P}}^*$  is the adjoint of  $\overline{\mathbb{P}}$ . Note that the orthogonality properties:

$$\overline{\mathbb{P}}\mathbf{G}' = 0, \quad (48)$$

$$\mathbf{G}'\overline{\mathbb{P}}^* = 0 \quad (49)$$

immediately follow from (47). In [37] it was shown, in the context of finite element approximations of the advection–diffusion equation, for the advection-dominated case, that the projector based on the  $H_0^1$ -inner product (termed the Dirichlet projector in [35]) produced a highly *localized* fine-scale Green's operator, despite the classical Green's operator being highly *non-local*. In fact, for the one-dimen-

sional case, the support of the fine-scale Green's operator was confined to individual elements, and there was no coupling between elements. It is important to realize that this is not a general feature of the fine-scale Green's operator, but one that depends crucially on the particular projector. For example, the fine-scale Green's operator produced by the  $L^2$ -projector was non-local in all cases.

Exact determination of the Green's function is not possible and neither is summing an infinite number of terms in the perturbation series. Consequently, two approximations are necessary in order to develop a practical solution scheme:

- (1) Approximation of the fine-scale Green's operator for the linearized Navier–Stokes system,  $\widehat{\mathbf{G}}'_{\overline{U}} \approx \mathbf{G}'_{\overline{U}}$ .
- (2) Approximation of the nonlinearities by truncation of the perturbation series.

Once these approximations are made precise, we have defined a turbulence model of the form (31). This will be discussed in the following section.

#### Remark

It needs to be emphasized that the pathway to an approximate turbulence model identified by the above assumptions is not the only possibility, but it does seem a viable candidate for LES-type modeling within the variational multiscale method. Clearly, a more direct attack on the fully nonlinear fine-scale equation, rather than the perturbation series approach, might seem an even more propitious approach. In either case, our theoretical framework for turbulence modeling remains (30) and (31).

### 3. Approximating the fine-scale Green's operator

A study of the fine-scale Green's operator for the linear, steady, advection–diffusion equation was performed in [37], in which an explicit formula was derived in terms of the classical Green's operator and a projector onto the coarse-scale space, given here by (47). It was shown that different projectors yielded very different locality properties of the fine-scale Green's operator. The  $H_0^1$ -projector produced a highly localized Green's operator, whereas the  $L^2$ -projector exhibited more global support. Locality is a very desirable property because it suggests local approximation, a significant simplification from the practical viewpoint. It has been known for some time that stabilization operators represent local approximations to fine-scale Green's operators (see [28,10,31,37]) and this also suggests that the product of stabilization operators and coarse-scale residuals would represent very simple but potentially effective representations of fine-scale fields. (A more precise justification of this idea for simple model problems was given in [37].)

So far, for the most part, effort devoted to calculating fine-scale Green's operators has utilized an analytical approach. This can only be executed rigorously in the simplest circumstances (see [28,10,31,37]), but provides

valuable insight and serves as a basis for comparing with approximate and more practically useful procedures. Given a fine-scale basis, and the variational equation for the fine-scale field, the fine-scale Green's operator can be computed (see [31]). However, heretofore no practical success has been attained with this approach because the functions used to represent the fine-scale basis, typically low-order polynomials, have not been able to faithfully describe advection-dominated asymptotic behavior, of paramount importance in high Reynolds and Péclet number applications. Recently, progress has been made by two of us (Cottrell and Hughes) utilizing the discontinuous variational multiscale method (see [38,9,13]). This approach provides considerable generality and enables fine-scales fields to be calculated numerically, accounting for nonlinearity, and time dependence. We believe it will represent an important step forward in better representing fine-scale fields, resulting in more accurate turbulence modeling procedures, and we hope to report on it in the near future.

In the present work we are content to work on the most simple and basic end of the approximation spectrum. The idea is to compute element-wise stabilization operators, denoted  $\tau$ , and calculate the fine-scale field as the product of  $\tau$  and the local coarse-scale residual,

$$\tilde{U}' \approx -\tau \text{Res}(\tilde{U}). \quad (50)$$

Note that  $\tau$  is matrix-valued in our case, specifically,  $\tau \in \mathbb{R}^{4 \times 4}$ , and it can be computed from the formula for the fine-scale Green's operator by assuming it takes the form of  $\tau$  times a Dirac distribution in each element. The result that ensues is that  $\tau$  is the element mean value of the fine-scale Green's operator. In the case of a space-time element,  $Q_n^e$ , we have (see [40])

$$\tau|_{Q^e} = \frac{1}{|Q^e|} \int_{Q^e} \int_{Q^e} \tilde{G}'_{\sim}(x, t; \hat{x}, \hat{t}) dQ d\hat{Q}. \quad (51)$$

Note that  $\tau$  is a function of  $\tilde{U}$ . This formula has been used to determine precise values of  $\tau$  for simple cases, primarily in the steady case, but, more often than not, well-established asymptotic scaling arguments have been used to directly calculate  $\tau$  in more complex circumstances. There are a number of references to this beginning with some of the earliest works on stabilized methods (see, e.g. [12,67,72,39,66,14,3]). This is the approach adopted here and the precise formula utilized is given in the following section.

Once we have a formula such as (50) we can construct the entire perturbation series approximation, as shown in [66,14]. However, in the present work, keeping with the theme of simplicity, we will truncate the series at the first term, namely (50).

Having described the simple path chosen in this work, we do wish to emphasize that we view it as extremely important to investigate other, richer possibilities within our theoretical framework of the fine-scale problem. We believe this will lead to practical and theoretical benefits.

## 4. Implementation

The space-time formulation of Section 2 is very general and is suggestive of a wide variety of interpretations. For fixed spatial domains semi-discrete formulations are very economical (see, e.g. [8]), and this is what is employed herein. In place of (20) and (22), we have, respectively,

$$\begin{aligned} B^h(W^h, U^h + U') &= L^h(W^h), \\ B^h(W^h, U^h + U') &= B_1^h(W^h, U^h) + B_2^h(W^h, U^h, U^h) + \tilde{B}_1^h(W^h, U') \\ &\quad + B_2^h(W^h, U^h, U') + B_2^h(W^h, U', U^h) \quad (\text{Cross stress}) \\ &\quad + B_2^h(W^h, U', U') \quad (\text{Reynolds stress}) \end{aligned} \quad (52)$$

where

$$L^h(W^h) = (w^h, f)_\Omega, \quad (54)$$

$$\begin{aligned} B_1^h(W^h, U^h) &= \left( w^h, \frac{\partial u^h}{\partial t} \right)_\Omega - (\nabla \cdot w^h, p^h)_\Omega \\ &\quad + (\nabla^s w^h, 2\nu \nabla^s u^h)_\Omega + (q^h, \nabla \cdot u^h)_\Omega, \end{aligned} \quad (55)$$

$$\tilde{B}_1^h(W^h, U') = -(\nabla \cdot w^h, p')_\Omega - (\nabla q^h, u')_\Omega, \quad (56)$$

$$B_2^h(W^h, U', U) = -(\nabla w^h, v \otimes u)_\Omega \quad (57)$$

and  $U^h = \{u^h, p^h\}$  and  $W^h = \{w^h, q^h\}$  have replaced  $\bar{U}$  and  $\bar{W}$ , respectively, and  $U'$  remains the same. The  $h$ -super-script denotes a mesh parameter. In this formulation, time is continuous at this stage. Eq. (53) is obtained by integrating by parts and invoking the following assumptions: (1)  $\frac{\partial w^h}{\partial t} = 0$ ; (2)  $u' = 0$  on  $\Gamma$ ; and (3)  $(\nabla^s w^h, 2\nu \nabla^s u')_\Omega = 0$ . The last assumption follows from the orthogonality conditions induced by the projector emanating from the bilinear form describing the viscous term (see [3,35,37]).

### 4.1. Fine-scale approximation

We assume that  $\Omega$  is partitioned into a set of subdomains, such as finite elements or NURBS elements, and on this partition we have a finite-dimensional space of functions, with local support, that is our approximation space defining  $U^h$  and  $W^h$ . Let  $x = \{x_i\}_{i=1}^3$ , denote the coordinates of element  $K$  in physical space, and let  $\xi = \{\xi_i\}_{i=1}^3$ , denote the coordinates of element  $\hat{K}$  in parametric space. Let  $x = x(\xi) : \hat{K} \rightarrow K$  be a continuously differentiable mapping with a continuously differentiable inverse. We now provide a detailed expression for the fine-scale approximation appearing in equation (50) for a typical element.

In the present notation,

$$U' \approx \tilde{U}' = \left\{ \begin{matrix} \tilde{u}' \\ \tilde{p}' \end{matrix} \right\} = -\tau \text{Res}(U^h), \quad (58)$$

where

$$\tau = \begin{bmatrix} \tau_M I_{3 \times 3} & \mathbf{0}_3 \\ \mathbf{0}_3^T & \tau_C \end{bmatrix}, \quad (59)$$



$$\mathbf{Res}(\mathbf{U}^h) = \left\{ \mathbf{r}_M(\mathbf{u}^h, p^h), \mathbf{r}_C(\mathbf{u}^h) \right\}, \quad (60)$$

$$\mathbf{r}_M(\mathbf{u}^h, p^h) = \frac{\partial \mathbf{u}^h}{\partial t} + \mathbf{u}^h \cdot \nabla \mathbf{u}^h + \nabla p^h - \nu \Delta \mathbf{u}^h - \mathbf{f}, \quad (61)$$

$$\mathbf{r}_C(\mathbf{u}^h) = \nabla \cdot \mathbf{u}^h, \quad (62)$$

$$\tau_M = \left( \frac{4}{\Delta t^2} + \mathbf{u}^h \cdot \mathbf{G} \mathbf{u}^h + C_I \nu^2 \mathbf{G} : \mathbf{G} \right)^{-1/2}, \quad (63)$$

$$\tau_C = (\tau_M \mathbf{g} \cdot \mathbf{g})^{-1}, \quad (64)$$

$$G_{ij} = \sum_{k=1}^3 \frac{\partial \xi_k}{\partial x_i} \frac{\partial \xi_k}{\partial x_j}, \quad (65)$$

$$\mathbf{G} : \mathbf{G} = \sum_{i,j=1}^3 G_{ij} G_{ij}, \quad (66)$$

$$\mathbf{u}^h \cdot \mathbf{G} \mathbf{u}^h = \sum_{i,j=1}^3 u_i^h G_{ij} u_j^h, \quad (67)$$

$$\mathbf{g}_i = \sum_{j=1}^3 \frac{\partial \xi_j}{\partial x_i}, \quad (68)$$

$$\mathbf{g} \cdot \mathbf{g} = \sum_{i=1}^3 g_i g_i \quad (69)$$

and  $\Delta t$  is the time step size and  $C_I$  is a positive constant, independent of the mesh size, derived from an element-wise inverse estimate (see, e.g. [45]). For a cube-shaped element, with  $h$  the edge length,  $G_{ij} = \frac{4}{h^2} \delta_{ij}$ , where  $\delta_{ij}$  is the Kronecker delta (i.e.,  $\delta_{ij} = 1$ , if  $i = j$ , and is zero otherwise).

$\tau_M$  is designed by asymptotic scaling arguments (see [2]) developed within the theory of stabilized methods (see, e.g. [32,67]).

#### Remarks

- (1) The momentum residual contains second derivatives of  $\mathbf{u}^h$  (i.e.,  $-\nu \Delta \mathbf{u}^h$ ). Typically,  $\mathbf{u}^h$  will be smooth on element interiors but may only be continuous across element interfaces. Interpreted distributionally, there are Dirac layers located on element interfaces. Jansen et al. [42] have developed a procedure for reconstructing second derivatives, avoiding the Dirac layers. The technique  $L^2$ -projects the first derivatives of  $\mathbf{u}^h$  onto the basis for  $\mathbf{u}^h$ . The derivatives of the projection are well defined on element interiors and, in particular, are square-integrable. We have used this procedure when  $\mathbf{u}^h$  is only continuous across element interfaces. However, our numerical experience indicated that if the nonlinear convergence tolerance within each time step was set sufficiently small, reconstructing second derivatives in this manner did not appreciably affect results. This observation is not consistent with those of Jansen et al. [42], and the matter deserves further study. When  $\mathbf{u}^h$  is at least  $C^1$ -continuous, it is of course not necessary to reconstruct second derivatives. This is the case for higher-order

NURBS utilized in our computations (see Sections 6 and 7).

- (2) Although we have not introduced the time discretization, the time step  $\Delta t$  appears in (63). For time steps of the order of the element advective time scale, that is,  $\Delta t = O(h/|\mathbf{u}^h|)$ , this behaves satisfactorily. However, as  $\Delta t \rightarrow 0$ , for fixed  $h/|\mathbf{u}^h|$ , the formulas for  $\tau_M$  and  $\tau_C$  degenerate in that  $\tau_M \rightarrow 0$  and  $\tau_C \rightarrow \infty$ . To address this deficiency, Codina et al. [16] have introduced the notion of “dynamic subgrid scales.” An ordinary differential equation and asymptotic scaling arguments are used to advance the fine-scale field. This means that the fine-scale field becomes a “history variable” that needs to be stored at each integration point. The computational structure is similar to that for inelastic constitutive equations in computational solid mechanics (see [70]). The procedure has been shown to be effective even for very small time steps. This seems like a promising step in the direction of more accurately representing the fine scales.
- (3) The definition of  $\tau_C$  derives from a discrete approximation of  $\nabla \cdot \mathcal{L}_{\text{ad}}^{-1} \nabla$ , where  $\mathcal{L}_{\text{ad}} = \partial/\partial t + \mathbf{u} \cdot \nabla - \nu \Delta$ . Note that  $\tau_M$  is the discrete approximation of  $\mathcal{L}_{\text{ad}}^{-1}$ .

Combining Eqs. (53) and (58), we obtain the following semi-discrete formulation: Find  $\mathbf{U}^h$  such that  $\forall \mathbf{W}^h$ ,

$$B^{MS}(\mathbf{W}^h, \mathbf{U}^h) - L^{MS}(\mathbf{W}^h) = 0, \quad (70)$$

where

$$\begin{aligned} B^{MS}(\mathbf{W}^h, \mathbf{U}^h) = & B^G(\mathbf{W}^h, \mathbf{U}^h) \\ & + (\mathbf{u}^h \cdot \nabla \mathbf{w}^h + \nabla q^h, \tau_M \mathbf{r}_M(\mathbf{u}^h, p^h))_\Omega \\ & + (\nabla \cdot \mathbf{w}^h, \tau_C \mathbf{r}_C(\mathbf{u}^h))_\Omega \\ & + (\mathbf{u}^h \cdot (\nabla \mathbf{w}^h)^T, \tau_M \mathbf{r}_M(\mathbf{u}^h, p^h))_\Omega \\ & - (\nabla \mathbf{w}^h, \tau_M \mathbf{r}_M(\mathbf{u}^h, p^h) \otimes \tau_M \mathbf{r}_M(\mathbf{u}^h, p^h))_\Omega, \end{aligned} \quad (71)$$

$$L^{MS}(\mathbf{W}^h) = (\mathbf{w}^h, \mathbf{f})_\Omega, \quad (72)$$

and

$$\begin{aligned} B^G(\mathbf{W}^h, \mathbf{U}^h) = & \left( \mathbf{w}^h, \frac{\partial \mathbf{u}^h}{\partial t} \right)_\Omega - (\nabla \mathbf{w}^h, \mathbf{u}^h \otimes \mathbf{u}^h)_\Omega \\ & - (\nabla \cdot \mathbf{w}^h, p^h)_\Omega + (q^h, \nabla \cdot \mathbf{u}^h)_\Omega \\ & + (\nabla^s \mathbf{w}^h, 2\nu \nabla^s \mathbf{u}^h)_\Omega. \end{aligned} \quad (73)$$

#### Remarks

- (1) The first term on the right-hand side of (71), and defined in (73), is the Galerkin term; the next two terms are classical stabilization terms; and the last two terms are the additional terms produced by the variational multiscale method. From this perspective, classical stabilization, such as SUPG and GLS (see [39]), is only a stepping stone toward the full variational multiscale method.

- (2) Another way to interpret (71) is to note that classical stabilization accounts for only one of the cross-stress terms, whereas the variational multiscale method accounts for both cross-stress and Reynolds-stress terms.

## 5. Time discretization and numerical implementation

In what follows,  $A$  is the nodal index in standard finite element analysis, and the control point index in NURBS-based isogeometric analysis, and  $\mathbf{e}_i$  is the  $i$ th Cartesian basis vector. We assume that velocity and pressure are expanded in terms of the same basis, denoted  $\{N_A\}_{A=1}^{n_b}$ , where  $n_b$  is the number of basis functions. This simplifies the exposition, but this is not a requirement of the method. Let  $\mathbf{V}$ ,  $\dot{\mathbf{V}}$ , and  $\mathbf{P}$  denote the vectors of nodal or control point degrees of freedom of velocity, velocity time derivative, and pressure, respectively. We define two residual vectors, corresponding to the momentum and continuity equations, by substituting  $N_A \mathbf{e}_i$  and  $N_A$  in place of  $\mathbf{w}^h$  and  $q^h$  in (70), respectively,

$$\mathbf{R}^M = [\mathbf{R}_{A,i}^M], \quad (74)$$

$$\mathbf{R}_{A,i}^M = B^{MS}(\{N_A \mathbf{e}_i, 0\}, \{\mathbf{u}^h, p^h\}) - L^{MS}(\{N_A \mathbf{e}_i, 0\}), \quad (75)$$

$$\mathbf{R}^C = [\mathbf{R}_A^C], \quad (76)$$

$$\mathbf{R}_A^C = B^{MS}(\{0, N_A\}, \{\mathbf{u}^h, p^h\}) - L^{MS}(\{0, N_A\}). \quad (77)$$

Although  $\dot{\mathbf{V}}$  is the time derivative of  $\mathbf{V}$ , we view it as independent in the time integration algorithm. We employ the generalized- $\alpha$  method, which was first applied to fluid dynamics in [43] (see also [15] for the original presentation for the equations of structural dynamics). Here we present the details of the algorithm for the equations of incompressible flow in the multiscale description. Our exposition is similar to that of Whiting and Jansen [76] and Whiting [75]. The algorithm is stated as follows: given  $\dot{\mathbf{V}}_n$ ,  $\mathbf{V}_n$ , find  $\dot{\mathbf{V}}_{n+1}$ ,  $\mathbf{V}_{n+1}$ ,  $\dot{\mathbf{V}}_{n+\alpha_m}$ ,  $\mathbf{V}_{n+\alpha_f}$ , and  $\mathbf{P}_{n+1}$ , such that

$$\mathbf{R}^M(\dot{\mathbf{V}}_{n+\alpha_m}, \mathbf{V}_{n+\alpha_f}, \mathbf{P}_{n+1}) = \mathbf{0}, \quad (78)$$

$$\mathbf{R}^C(\dot{\mathbf{V}}_{n+\alpha_m}, \mathbf{V}_{n+\alpha_f}, \mathbf{P}_{n+1}) = \mathbf{0}, \quad (79)$$

$$\mathbf{V}_{n+1} = \mathbf{V}_n + \Delta t \dot{\mathbf{V}}_n + \gamma \Delta t (\dot{\mathbf{V}}_{n+1} - \dot{\mathbf{V}}_n), \quad (80)$$

$$\dot{\mathbf{V}}_{n+\alpha_m} = \dot{\mathbf{V}}_n + \alpha_m (\dot{\mathbf{V}}_{n+1} - \dot{\mathbf{V}}_n), \quad (81)$$

$$\mathbf{V}_{n+\alpha_f} = \mathbf{V}_n + \alpha_f (\mathbf{V}_{n+1} - \mathbf{V}_n), \quad (82)$$

where  $\Delta t = t_{n+1} - t_n$  is the time step size, and  $\alpha_m$ ,  $\alpha_f$ , and  $\gamma$  are real-valued parameters that define the method. Given the solution at time level  $t_n$ , we integrate the equations of motion to the time level  $t_{n+1}$  by forcing the residuals of the momentum and continuity equations, (78) and (79), to vanish. Parameters  $\alpha_m$ ,  $\alpha_f$ , and  $\gamma$  are selected based on considerations of accuracy and stability. It was shown in [43] that second-order accuracy in time is achieved if

$$\gamma = 1/2 + \alpha_m - \alpha_f, \quad (83)$$

while unconditional stability is attained if

$$\alpha_m \geq \alpha_f \geq 1/2. \quad (84)$$

We obtain a one-parameter family of second-order accurate and unconditionally stable time integration schemes

by setting  $\gamma$  according to (83) and employing the following parameterization of the intermediate time levels:

$$\alpha_m = \frac{1}{2} \left( \frac{3 - \rho_\infty}{1 + \rho_\infty} \right) \quad \text{and} \quad \alpha_f = \frac{1}{1 + \rho_\infty}, \quad (85)$$

where the parameter  $\rho_\infty$  is the spectral radius of the amplification matrix as  $\Delta t \rightarrow \infty$ , which controls high-frequency dissipation (see [29]). To solve the nonlinear system of equations (78)–(82), we employ Newton's method, which results in a two-stage predictor–multicorrector algorithm.

### Predictor stage

Set

$$\mathbf{V}_{n+1,(0)} = \mathbf{V}_n, \quad (86)$$

$$\dot{\mathbf{V}}_{n+1,(0)} = \frac{(\gamma - 1)}{\gamma} \dot{\mathbf{V}}_n, \quad (87)$$

$$\mathbf{P}_{n+1,(0)} = \mathbf{P}_n, \quad (88)$$

where subscript 0 on the left-hand side quantities is the iteration index. This was referred to as the “same velocity” predictor by Jansen et al. [43], and was shown to be efficient for turbulence applications. The factor  $(\gamma - 1)/\gamma$  makes the predictor consistent with the generalized- $\alpha$  equations.

### Multi-corrector stage

Repeat the following steps for  $l = 1, 2, \dots, l_{\max}$ .

- (1) Evaluate iterates at the intermediate time levels,

$$\dot{\mathbf{V}}_{n+\alpha_m,(l)} = \dot{\mathbf{V}}_n + \alpha_m (\dot{\mathbf{V}}_{n+1,(l-1)} - \dot{\mathbf{V}}_n), \quad (89)$$

$$\mathbf{V}_{n+\alpha_f,(l)} = \mathbf{V}_n + \alpha_f (\mathbf{V}_{n+1,(l-1)} - \mathbf{V}_n), \quad (90)$$

$$\mathbf{P}_{n+1,(l)} = \mathbf{P}_{n+1,(l-1)}. \quad (91)$$

Note (89) and (90) amount to satisfaction of (81) and (82).

- (2) Use the intermediate solutions to assemble the residuals of the continuity and momentum equations and the corresponding matrices in the linear system:

$$\mathbf{K}_{(l)} \Delta \dot{\mathbf{V}}_{n+1,(l)} + \mathbf{G}_{(l)} \Delta \mathbf{P}_{n+1,(l)} = -\mathbf{R}_{(l)}^M, \quad (92)$$

$$\mathbf{D}_{(l)} \Delta \dot{\mathbf{V}}_{n+1,(l)} + \mathbf{L}_{(l)} \Delta \mathbf{P}_{n+1,(l)} = -\mathbf{R}_{(l)}^C. \quad (93)$$

Solve this linear system using a preconditioned GMRES algorithm (see [64]) to a specified tolerance. Note that in (92) and (93) we are solving for the increment in  $\dot{\mathbf{V}}$  rather than  $\mathbf{V}$ .

- (3) Having solved the linear system, update the iterates:

$$\dot{\mathbf{V}}_{n+1,(l)} = \dot{\mathbf{V}}_{n+1,(l-1)} + \Delta \dot{\mathbf{V}}_{n+1,(l)}, \quad (94)$$

$$\mathbf{V}_{n+1,(l)} = \mathbf{V}_{n+1,(l-1)} + \gamma \Delta t \Delta \dot{\mathbf{V}}_{n+1,(l)}, \quad (95)$$

$$\mathbf{P}_{n+1,(l)} = \mathbf{P}_{n+1,(l-1)} + \Delta \mathbf{P}_{n+1,(l)}. \quad (96)$$

Note, this update automatically satisfies (80). This completes one nonlinear iteration.

Two to four nonlinear iterations are typically required to achieve convergence in a time step.

The most computationally involved part of the above algorithm is obviously step (2) of the multi-corrector stage. The amount of computational work required is equivalent to the solution of a linear finite element problem, which involves assembling the left-hand side matrices and right-hand side vectors, and calling a linear equation solver. Implementation in the isogeometric analysis setting is very similar to that of standard finite elements (see [30] for details).

The matrices in (92) and (93) are approximations of the consistent tangent matrices, given by partial differentiation, namely

$$\begin{aligned} K_{(l)} &= \frac{\partial R^M(\dot{V}_{n+\alpha_m}, V_{n+\alpha_f}, P_{n+1})}{\partial \dot{V}_{n+\alpha_m}} \frac{\partial \dot{V}_{n+\alpha_m}}{\partial \dot{V}_{n+1}} \\ &+ \frac{\partial R^M(\dot{V}_{n+\alpha_m}, V_{n+\alpha_f}, P_{n+1})}{\partial V_{n+\alpha_f}} \frac{\partial V_{n+\alpha_f}}{\partial \dot{V}_{n+1}} \\ &= \alpha_m \frac{\partial R^M(\dot{V}_{n+\alpha_m}, V_{n+\alpha_f}, P_{n+1})}{\partial \dot{V}_{n+\alpha_m}} \\ &+ \alpha_f \gamma \Delta t \frac{\partial R^M(\dot{V}_{n+\alpha_m}, V_{n+\alpha_f}, P_{n+1})}{\partial V_{n+\alpha_f}}, \end{aligned} \quad (97)$$

$$G_{(l)} = \frac{\partial R^M(\dot{V}_{n+\alpha_m}, V_{n+\alpha_f}, P_{n+1})}{\partial P_{n+1}}, \quad (98)$$

$$\begin{aligned} D_{(l)} &= \frac{\partial R^C(\dot{V}_{n+\alpha_m}, V_{n+\alpha_f}, P_{n+1})}{\partial \dot{V}_{n+\alpha_m}} \frac{\partial \dot{V}_{n+\alpha_m}}{\partial \dot{V}_{n+1}} \\ &+ \frac{\partial R^C(\dot{V}_{n+\alpha_m}, V_{n+\alpha_f}, P_{n+1})}{\partial V_{n+\alpha_f}} \frac{\partial V_{n+\alpha_f}}{\partial \dot{V}_{n+1}} \\ &= \alpha_m \frac{\partial R^C(\dot{V}_{n+\alpha_m}, V_{n+\alpha_f}, P_{n+1})}{\partial \dot{V}_{n+\alpha_m}} \\ &+ \alpha_f \gamma \Delta t \frac{\partial R^C(\dot{V}_{n+\alpha_m}, V_{n+\alpha_f}, P_{n+1})}{\partial V_{n+\alpha_f}}, \end{aligned} \quad (99)$$

$$L_{(l)} = \frac{\partial R^C(\dot{V}_{n+\alpha_m}, V_{n+\alpha_f}, P_{n+1})}{\partial P_{n+1}}. \quad (100)$$

In obtaining (97) and (99), we used (80)–(82).

Explicit formulas for the matrices used in our calculations are given as follows:

$$K = [K_{AB}^{ij}], \quad (101)$$

$$\begin{aligned} K_{AB}^{ij} &= \alpha_m (N_A, N_B)_\Omega \delta_{ij} + \alpha_m (\mathbf{u}^h \cdot \nabla N_A \tau_M, N_B)_\Omega \delta_{ij} \\ &+ \alpha_f \gamma \Delta t (N_A, \mathbf{u}^h \cdot \nabla N_B)_\Omega \delta_{ij} + \alpha_f \gamma \Delta t (\nabla N_A v, \nabla N_B)_\Omega \delta_{ij} \\ &+ \alpha_f \gamma \Delta t (\nabla N_A \cdot \mathbf{e}_j v, \nabla N_B \cdot \mathbf{e}_i)_\Omega \\ &+ \alpha_f \gamma \Delta t (\mathbf{u}^h \cdot \nabla N_A \tau_M, \mathbf{u}^h \cdot \nabla N_B)_\Omega \delta_{ij} \\ &+ \alpha_f \gamma \Delta t (\nabla N_A \cdot \mathbf{e}_i \tau_C, \nabla N_B \cdot \mathbf{e}_j)_\Omega, \end{aligned} \quad (102)$$

$$G = [G_{AB}^i], \quad (103)$$

$$G_{AB}^i = -(\nabla N_A \cdot \mathbf{e}_i, N_B)_\Omega + (\mathbf{u}^h \cdot \nabla N_A \mathbf{e}_i \tau_M, \nabla N_B)_\Omega, \quad (104)$$

$$D = [D_{AB}^i], \quad (105)$$

$$\begin{aligned} D_{AB}^i &= \alpha_f \gamma \Delta t (N_A, \nabla N_B \cdot \mathbf{e}_i)_\Omega \\ &+ \alpha_f \gamma \Delta t (\nabla N_A \tau_M, \mathbf{u}^h \cdot \nabla N_B \mathbf{e}_i)_\Omega \\ &+ \alpha_m (\nabla N_A \tau_M, N_B \mathbf{e}_i)_\Omega \end{aligned} \quad (106)$$

and

$$L = [L_{AB}], \quad (107)$$

$$L_{AB} = (\nabla N_A \tau_M, \nabla N_B)_\Omega, \quad (108)$$

where  $\delta_{ij}$  is the Kronecker delta, and the iteration index  $l$  has been omitted to simplify the notation.

## 6. Forced isotropic turbulence

### 6.1. Discretization

The domain in physical space is  $\Omega = (2\pi)^3$  with periodic boundary conditions in all directions. We employ uniform meshes of NURBS basis functions. The functions are constructed in the usual tensor product format [30]. We employ meshes of  $32^3$ ,  $64^3$ ,  $128^3$ , and  $256^3$  elements and basis functions, which are equal in number due to periodicity. An illustration of the basis functions for an 8 element mesh in one dimension is presented in Fig. 3. For a fixed order we study the effect of  $h$ -refinement, that is, we subdivide meshes. For a fixed mesh we study the effect of  $k$ -refinement, that is, we elevate order. Notice that in the  $k$ -refinement process, the number of degrees-of-freedom is the same for every order. This is due to the full periodicity of the basis.

### 6.2. Phase-error analysis for classical finite elements and NURBS

#### 6.2.1. The first-order wave equation

To determine the performance of NURBS applied to flow problems, a natural starting point is the first-order wave equation, or pure advection. Here we compare *analytic* solutions to the discrete equations arrived at by finite element and NURBS treatments of the problem.

A linear dispersive system is one that admits solutions of the form (see [74]):

$$\phi = a \cos(kx - \omega t), \quad (109)$$

where the frequency  $\omega$  is a real function of the wavenumber  $k$ , with the specific form of  $\omega(k)$  being determined by the system. If the phase speed  $\omega(k)/k$  depends on  $k$ , rather than being a constant, the system is said to be “dispersive”. For the first-order wave equation posed on an infinite domain, namely,

$$\frac{\partial \phi}{\partial t} + u \frac{\partial \phi}{\partial x} = 0, \quad \text{for } x \in ]-\infty, +\infty[, \quad (110)$$

$\omega = ku$ , and any dispersion in a numerical solution is artificial. That is, every Fourier mode should travel to the right

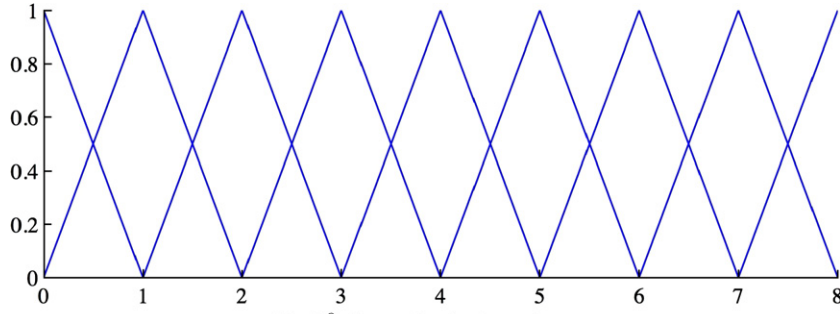
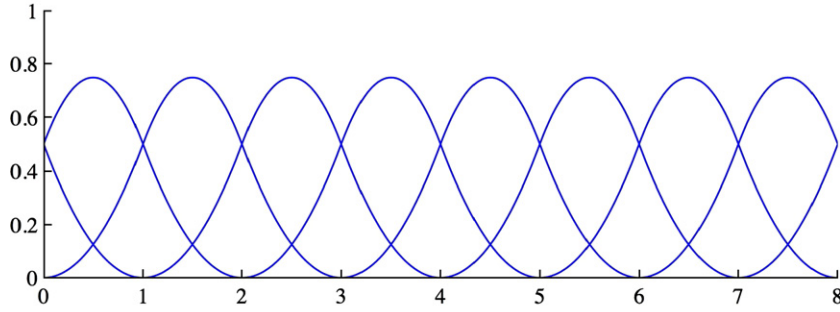
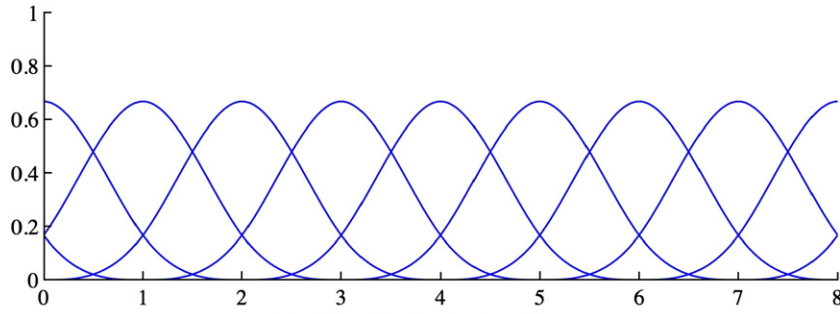
(a)  $C^0$ -linear basis functions.(b)  $C^1$ -quadratic basis functions.(c)  $C^2$ -cubic basis functions.

Fig. 3. One-dimensional periodic basis functions.

at speed  $u$  (i.e., pure advection), any deviations being artifacts of the numerics.

For both finite elements and NURBS, we seek a solution of the form

$$\phi = \sum_{A=1}^{n_b} \phi_A(t) N_A(x). \quad (111)$$

In the case where  $N_A$  is a standard finite element basis function, we associate its coefficient  $\phi_A$  with the value of the function at the node  $x_A$ . For the non-interpolatory NURBS basis,  $\phi_A$  is still the coefficient of function  $N_A$ , but the nodal value interpretation no longer holds. Still, we may speak of a “stencil” in the usual way (though perhaps the specific choice of terminology is less appropriate). To arrive at a stencil for either finite elements or NURBS, we substitute (111) into (110), multiply by basis function  $N_A$ , and integrate to get

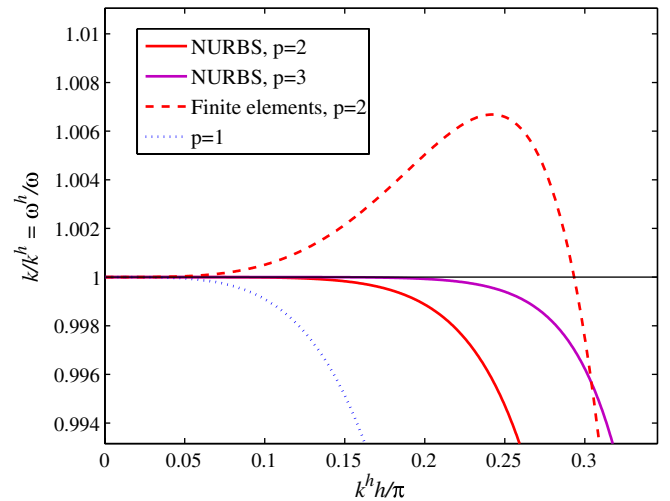


Fig. 4. The first-order wave equation. Phase errors versus non-dimensional wave numbers. Comparison of linear and quadratic finite elements,  $C^1$  quadratic NURBS, and  $C^2$  cubic NURBS.



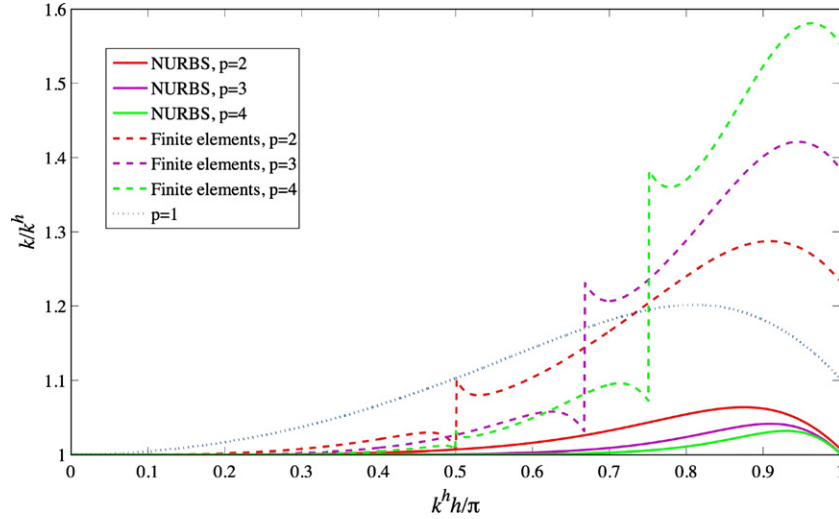


Fig. 5. The heat equation. Phase errors versus non-dimensional wave numbers. Comparison of classical  $C^0$ -continuous finite elements and NURBS for  $p = 1-4$ .

$$\int_0^L N_A \sum_{B=1}^{m_b} (\dot{\phi}_B N_B + u \phi_B N'_B) dx = 0, \quad (112)$$

where the superposed dot denotes differentiation with respect to  $t$  and the prime superscript denotes differentiation with respect to  $x$ .

Linear finite elements and linear NURBS are identical, so we begin our investigation with the quadratic case. Assume a uniform mesh with element length  $h$ . Looking first at the case where the  $N_A$ 's are  $C^1$  quadratic NURBS functions (actually, B-splines in this simple scenario), performing the integration in (112) yields

$$\begin{aligned} & \frac{1}{120} (\dot{\phi}_{A-2} + 26\dot{\phi}_{A-1} + 66\dot{\phi}_A + 26\dot{\phi}_{A+1} + \dot{\phi}_{A+2}) \\ & + \frac{u}{24h} (-\phi_{A-2} - 10\phi_{A-1} + 10\phi_{A+1} + \phi_{A+2}) = 0. \end{aligned} \quad (113)$$

As in [73], we let

$$\phi_A = \exp i(k^h A h - \omega t) \quad (114)$$

where  $k^h$  is the discrete wave number, an approximation to  $k = \omega/u$ , and  $i = \sqrt{-1}$ . Substituting this into (113) and simplifying yields

$$\begin{aligned} & \frac{-1\omega}{120} (e^{-2i\theta} + 26e^{-i\theta} + 66 + 26e^{i\theta} + e^{2i\theta}) \\ & + \frac{u}{24h} (-e^{-2i\theta} - 10e^{-i\theta} + 10e^{i\theta} + e^{2i\theta}) = 0, \end{aligned} \quad (115)$$

where  $\theta = k^h h$ . Rearranging and recalling that  $(e^{i\alpha} + e^{-i\alpha})/2 = \cos \alpha$  and  $(e^{i\alpha} - e^{-i\alpha})/2i = \sin \alpha$  we get

$$\omega(\cos 2\theta + 26 \cos \theta + 33) - \frac{5u}{h} (\sin 2\theta + 10 \sin \theta) = 0. \quad (116)$$

Finally, solving for  $k/k^h = \omega^h/\omega$  gives us

$$\frac{k}{k^h} = \frac{5(10 \sin \theta + \sin 2\theta)}{\theta(33 + 26 \cos \theta + \cos 2\theta)}. \quad (117)$$

For the classical quadratic finite element (see [29]), the situation is more complicated as the basis function  $N_A$  can take on two forms. If  $N_A$  corresponds to an end node (i.e.,  $A$  odd), then performing the integration in (112) results in

$$\begin{aligned} & \frac{1}{10} (-\dot{\phi}_{A-2} + 2\dot{\phi}_{A-1} + 8\dot{\phi}_A + 2\dot{\phi}_{A+1} - \dot{\phi}_{A+2}) \\ & + 2u \frac{\phi_{A+1} - \phi_{A-1}}{2h} - u \frac{\phi_{A+2} - \phi_{A-2}}{4h} = 0. \end{aligned} \quad (118)$$

For the case where  $N_A$  is associated with a center node (i.e.,  $A$  even), performing the same steps yields

$$\frac{1}{10} (\dot{\phi}_{A-1} + 8\dot{\phi}_A + \dot{\phi}_{A+1}) + u \frac{\phi_{A+1} - \phi_{A-1}}{2h} = 0. \quad (119)$$

Following Gresho and Sani [23], we let

$$\phi_A(t) = \left[ \frac{1 + (-1)^A}{2} + \beta \frac{1 - (-1)^A}{2} \right] \exp i(k^h A h - \omega t). \quad (120)$$

Substituting (120) into (119), solving the latter for  $\beta$  and using that result in (118), we arrive at<sup>5</sup>

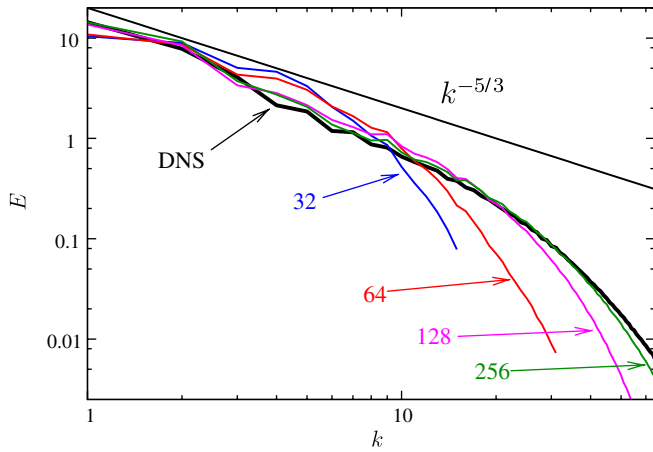
$$\frac{k}{k^h} = \frac{-2 \sin 2\theta \pm \sqrt{(1 - \cos 2\theta)(19 - \cos 2\theta)}}{\theta(3 - \cos 2\theta)}. \quad (121)$$

See [23] for a discussion on selecting “+” or “−” in (121). Plots of the phase error  $k/k^h = \omega^h/\omega$  for these two quadratic cases, as well as  $C^2$  cubic NURBS and linears, are shown in Fig. 4. We see that the quadratic finite elements actually overshoot the exact solution for part of the domain whereas the NURBS solution is considerably more accurate. The cubic NURBS are better still. For a fixed

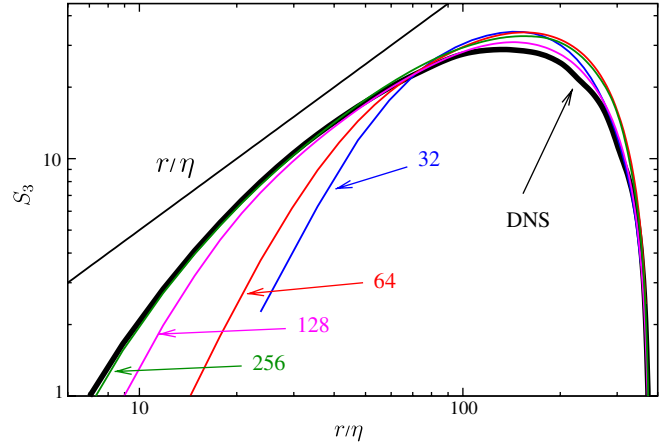
<sup>5</sup> Note that if we had considered  $C^0$  quadratic NURBS instead of  $C^1$  quadratic finite elements, the stencil would have been different, but the results for  $\omega$  would be exactly the same. This is because  $C^0$  NURBS basis functions are different from the classical finite element basis functions, but the *space* they span is exactly the same.

wavenumber, the error in the phase speed goes as  $O(h^4)$  for  $C^0$  quadratic finite elements and as  $O(h^6)$  for the  $C^1$  quadratic NURBS. In general, the error is  $O(h^{2p})$  for classical  $C^0$  finite elements of order  $p$ ,  $p > 1$ , and  $O(h^{2p+2})$  for  $C^{p-1}$  NURBS of order  $p$ ,  $p \geq 1$  (see [73]). Note, this acknowl-

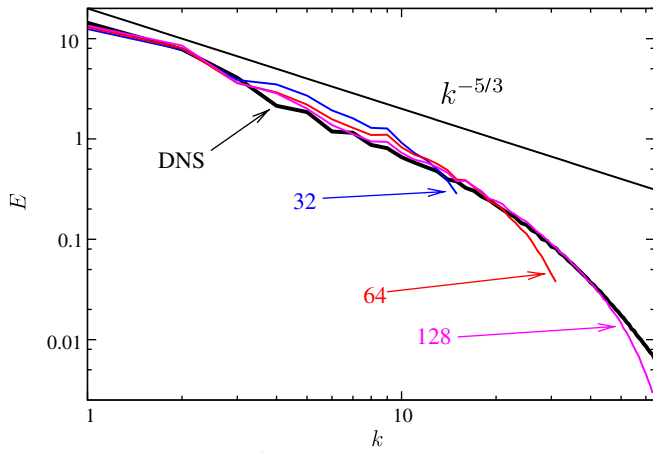
edges the fact that linear finite elements, that is,  $p = 1$ , are superconvergent, in that they achieve  $O(h^4)$  phase error (see [23]). These results illustrate the superiority of NURBS over classical finite elements for advective processes governed by the first-order wave equation.



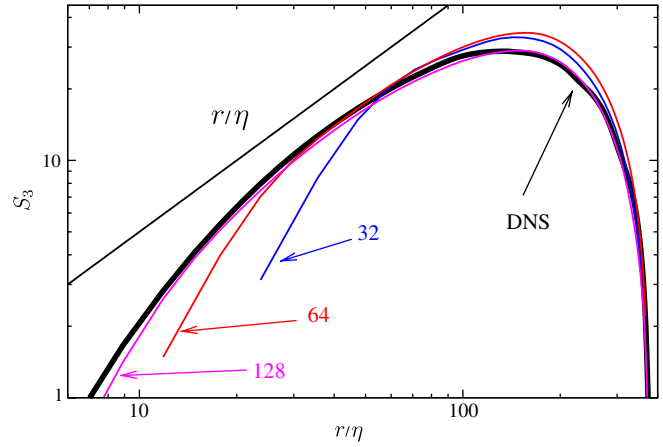
(a)  $C^0$ -continuous linear NURBS



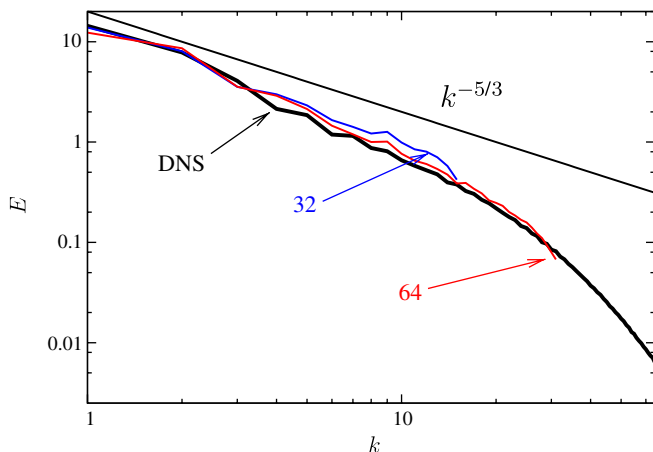
(a)  $C^0$ -continuous linear NURBS



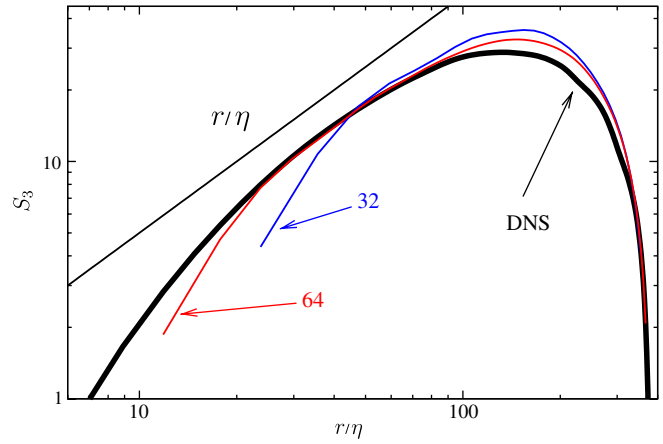
(b)  $C^1$ -continuous quadratic NURBS



(b)  $C^1$ -continuous quadratic NURBS



(c)  $C^2$ -continuous cubic NURBS



(c)  $C^2$ -continuous cubic NURBS

Fig. 6. Energy spectra for  $h$ -refinement.  $Re_\lambda = 165$ .

Fig. 7. Two-point third-order structure functions for  $h$ -refinement.  $Re_\lambda = 165$ .

### 6.2.2. The heat equation

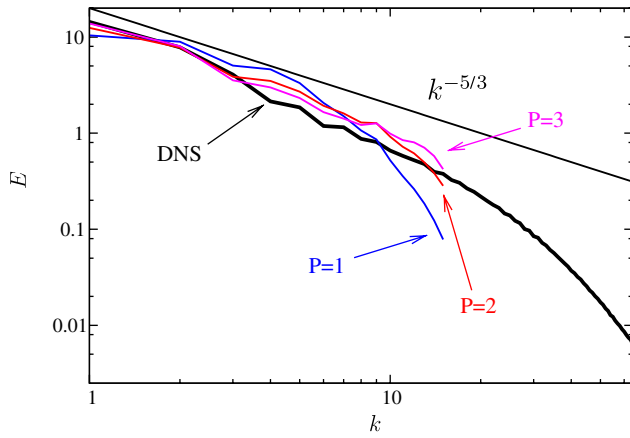
We study the heat equation given by

$$\frac{\partial \phi}{\partial t} = \kappa \frac{\partial^2 \phi}{\partial x^2}, \quad \text{for } x \in ]-\infty, +\infty[ \quad (122)$$

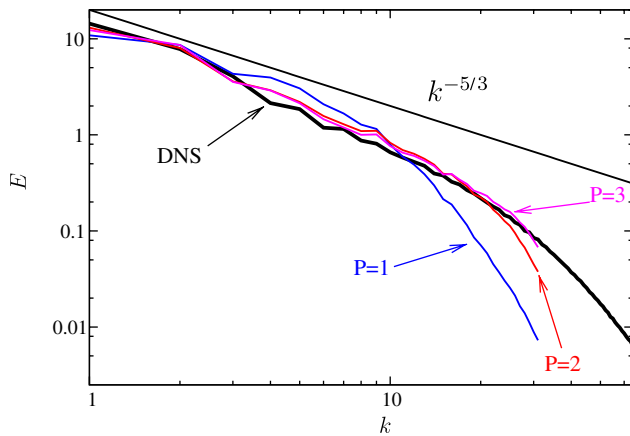
and proceed as in the case of the first-order wave equation, except this time we assume

$$\phi_A = \exp(ik^h Ah - \omega t). \quad (123)$$

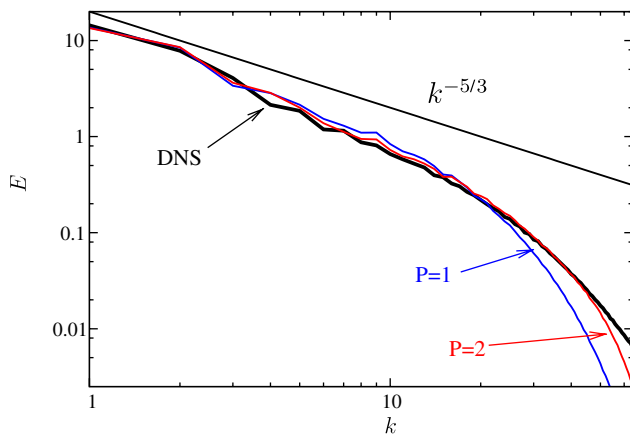
The dispersion analysis is performed for finite elements and NURBS using basis functions of order  $p = 2$  through  $p = 4$ . For completeness, the solution using linear elements is shown as well, though for linear elements there is no



(a) Meshes of  $32^3$  elements

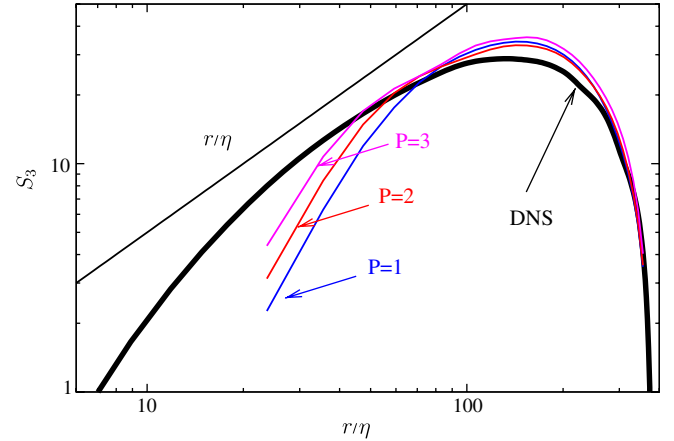


(b) Meshes of  $64^3$  elements

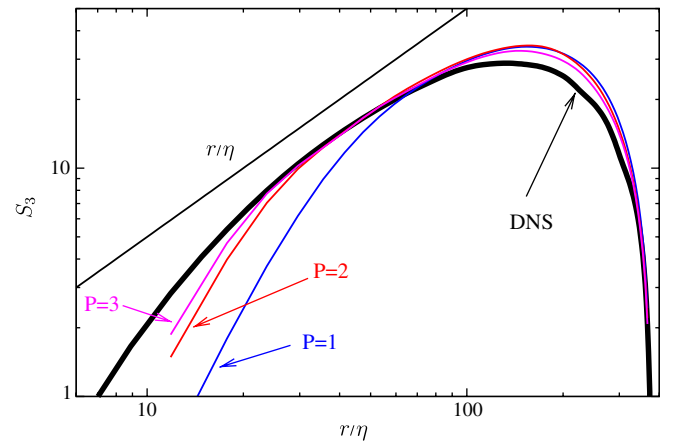


(c) Meshes of  $128^3$  elements

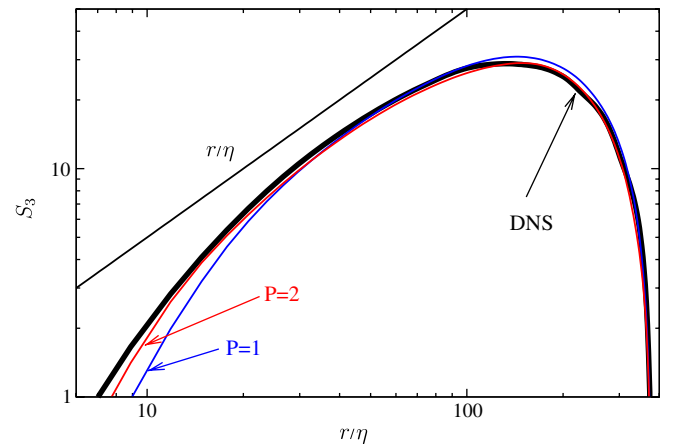
Fig. 8. Energy spectra for  $k$ -refinement.  $Re_\lambda = 165$ .



(a) Meshes of  $32^3$  elements



(b) Meshes of  $64^3$  elements



(c) Meshes of  $128^3$  elements

Fig. 9. Two-point third-order structure functions for  $k$ -refinement.  $Re_\lambda = 165$ .

difference between finite elements and NURBS. Results are presented in Fig. 5.

The superior behavior of NURBS basis functions compared with finite elements is once again evident. In this

case, the finite element results depict an accurate acoustical branch and inaccurate optical branches (see [11]). It is very important to observe the trends in Fig. 5. For finite elements, the optical branches *diverge* as  $p$  is increased.

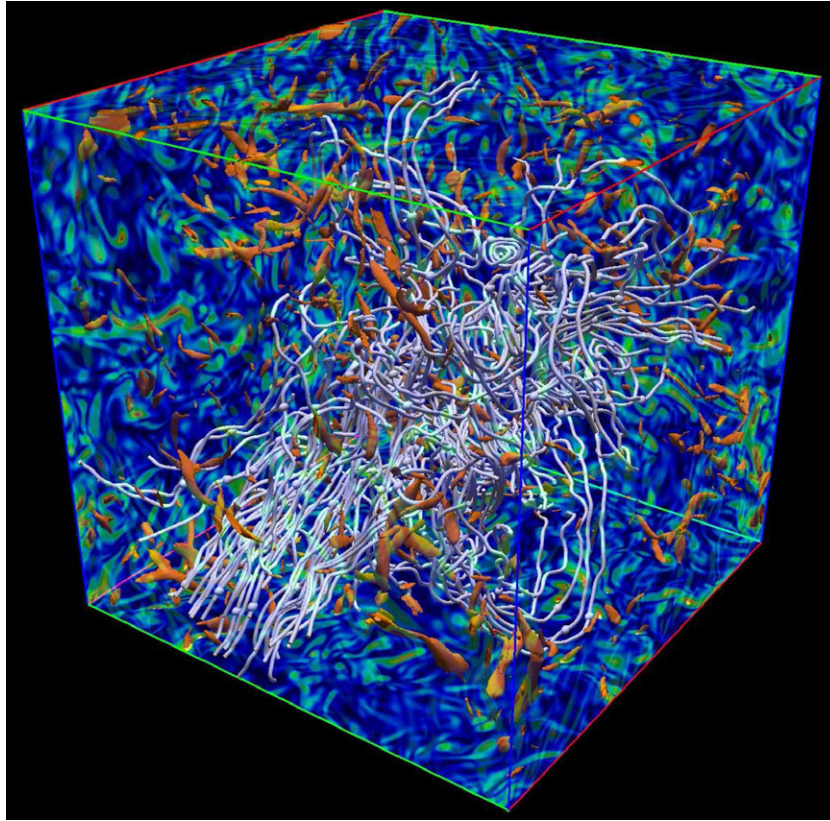


Fig. 10. Vorticity isosurfaces, velocity streamlines, and vorticity contours plotted on the entire computational domain for  $Re_\lambda = 165$ .

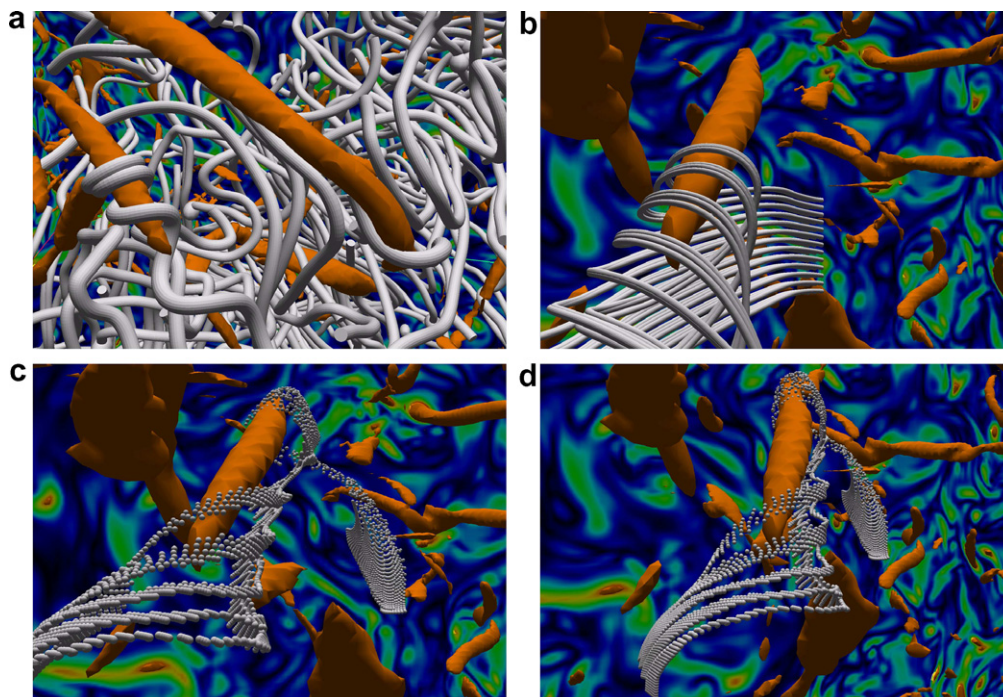


Fig. 11. Vorticity isosurfaces, velocity streamlines, and vorticity contours for  $Re_\lambda = 165$ . Detail of the local vortical structures.



That is, the errors in the higher wave numbers become greater as  $p$  is increased. On the other hand, for NURBS, the entire spectrum converges as  $p$  is increased. These opposite trends are likely very important in applications in which the entire discrete spectrum participates significantly in the solution. These results demonstrate the superiority of NURBS over classical finite elements for diffusive processes governed by the heat equation. The combination of results for advective and diffusive processes suggest to us that NURBS may be capable of attaining better accuracy than classical finite elements in representing turbulence. (A companion study in which turbulent channel flows were computed using standard quadratic finite elements and quadratic  $C^1$  NURBS has confirmed this behavior. See [1].)

### 6.3. Constant power-input forcing

We simulate forced isotropic turbulence by supplying a constant power input in the lowest velocity modes. The force at each instant is given by

$$\mathbf{f}(\mathbf{x}) = \sum_{\substack{|\mathbf{k}_i| < k_f \\ \mathbf{k} \neq \mathbf{0}}} \frac{P_{\text{in}}}{2E_{k_f}} \hat{\mathbf{u}}_{\mathbf{k}} \exp(\mathbf{i}\mathbf{k} \cdot \mathbf{x}) \quad (124)$$

where  $\mathbf{i} = \sqrt{-1}$ ,  $P_{\text{in}}$  is the fixed power input, set to 62.8436001234 in the simulations,

$$E_{k_f} = \frac{1}{2} \sum_{\substack{|\mathbf{k}_i| < k_f \\ \mathbf{k} \neq \mathbf{0}}} \hat{\mathbf{u}}_{\mathbf{k}} \cdot \hat{\mathbf{u}}_{\mathbf{k}} \quad (125)$$

is the kinetic energy contained in the lowest modes, and

$$\hat{\mathbf{u}}_{\mathbf{k}} = \frac{1}{|\Omega|} \int_{\Omega} \mathbf{u}^h(\mathbf{x}) \exp(-\mathbf{i}\mathbf{k} \cdot \mathbf{x}) d\Omega \quad (126)$$

denote the Fourier coefficients of the velocity field. The  $\hat{\mathbf{u}}_{\mathbf{k}}$  are computed for each  $\mathbf{k}$  that satisfies  $|\mathbf{k}_i| < k_f$ ,  $i = 1, 2, 3$ .  $k_f$  is selected to be 3 in our calculations. The integrals in (126) are computed by quadrature rather than by fast Fourier transforms because only a few modes are required.

The solution may be written as

$$\mathbf{u}^h = \sum_A N_A \mathbf{d}_A \quad (127)$$

where  $N_A$ 's are the basis functions and  $\mathbf{d}_A$ 's are the degrees of freedom, and thus it follows that the Fourier coefficients can be written as a matrix–vector product,

$$\begin{aligned} \hat{\mathbf{u}}_{\mathbf{k}} &= \frac{1}{|\Omega|} \int_{\Omega} \mathbf{u}^h(\mathbf{x}) \exp(-\mathbf{i}\mathbf{k} \cdot \mathbf{x}) d\Omega \\ &= \frac{1}{|\Omega|} \int_{\Omega} \sum_A N_A(\mathbf{x}) \mathbf{d}_A \exp(-\mathbf{i}\mathbf{k} \cdot \mathbf{x}) d\Omega \\ &= \sum_A \left[ \frac{1}{|\Omega|} \int_{\Omega} N_A(\mathbf{x}) \exp(-\mathbf{i}\mathbf{k} \cdot \mathbf{x}) d\Omega \right] \mathbf{d}_A \\ &= \sum_A B_{\mathbf{k},A} \mathbf{d}_A \end{aligned} \quad (128)$$

in which  $B_{\mathbf{k},A}$  can be precomputed.

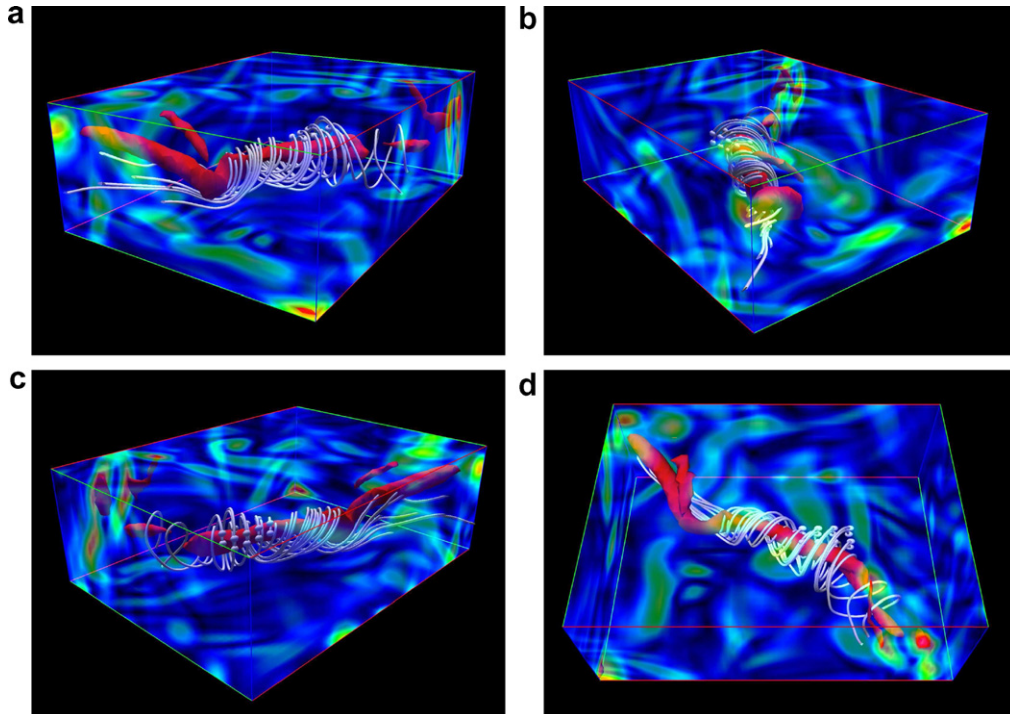


Fig. 12. Vorticity isosurfaces, velocity streamlines, and vorticity contours for  $Re_{\lambda} = 165$ . Detail of a single vortical structure.

#### 6.4. Test cases

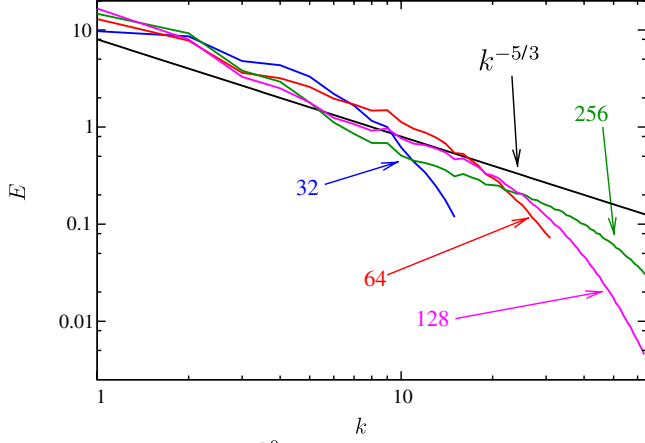
We consider two cases,  $Re_\lambda = 165$  and  $Re_\lambda = \infty$ , where  $Re_\lambda$  is the Taylor microscale Reynolds number [58].

For  $Re_\lambda = 165$  the kinematic viscosity,  $\nu$ , is set to  $1/150$ . The kinetic energy is computed as

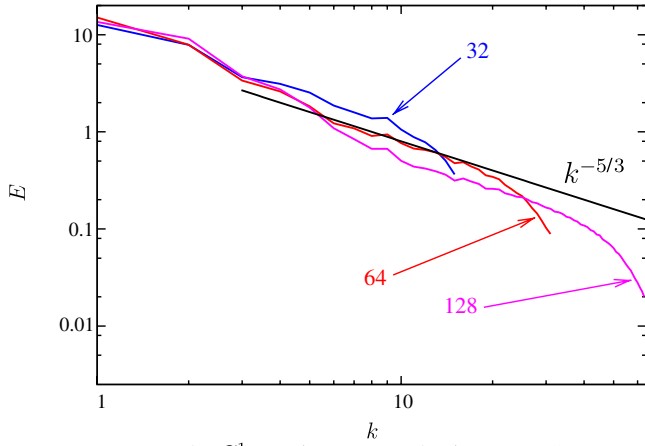
$$q^2 = \frac{1}{2|\Omega|} \int_{\Omega} \mathbf{u}^h(\mathbf{x}) \cdot \mathbf{u}^h(\mathbf{x}) d\Omega \quad (129)$$

which fluctuates about 41,  $\pm 15\%$ , in all cases. Thus,

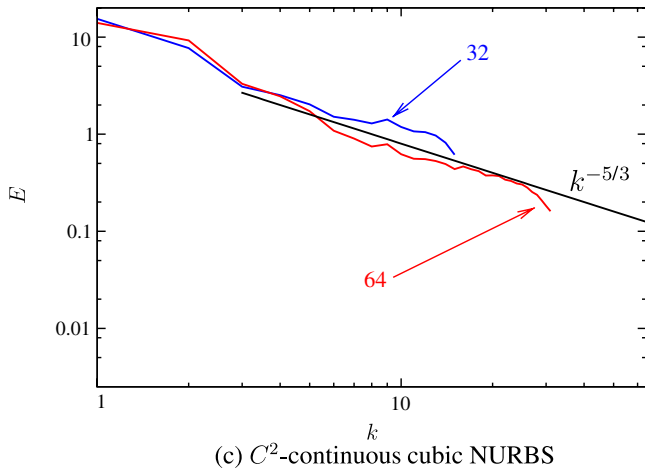
$$Re_\lambda = \frac{2q^2}{3} \sqrt{\frac{15}{\epsilon \nu}} \quad (130)$$



(a)  $C^0$ -continuous linear NURBS

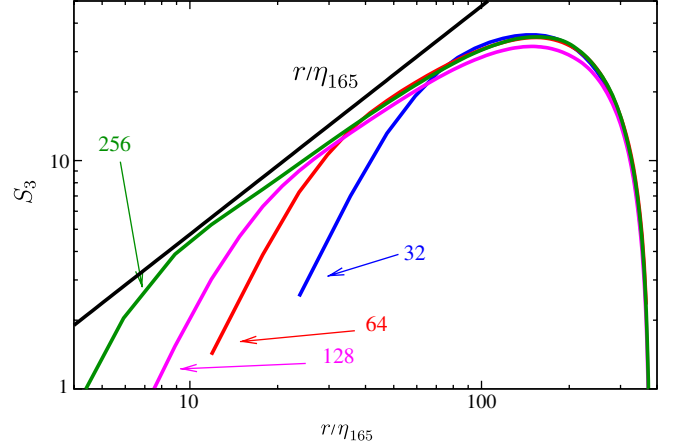


(b)  $C^1$ -continuous quadratic NURBS

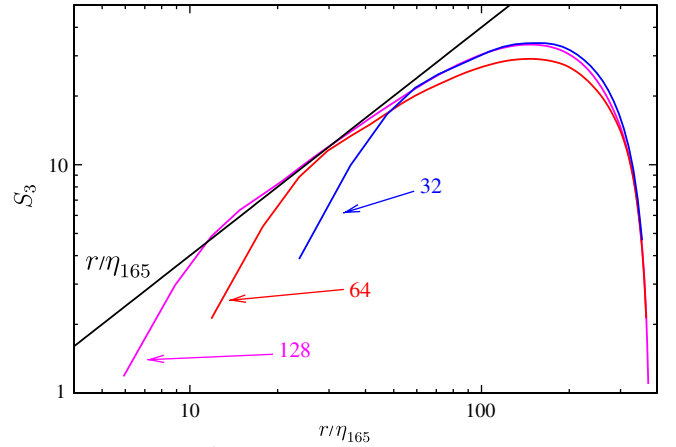


(c)  $C^2$ -continuous cubic NURBS

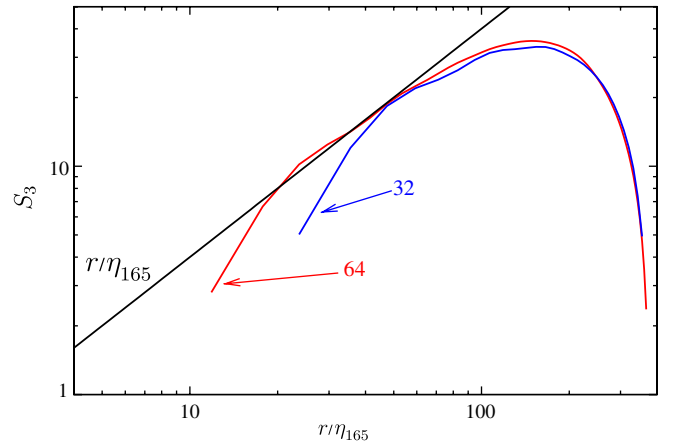
Fig. 13. Energy spectra for  $h$ -refinement.  $Re_\lambda = \infty$ .



(a)  $C^0$ -continuous linear NURBS



(b)  $C^1$ -continuous quadratic NURBS



(c)  $C^2$ -continuous cubic NURBS

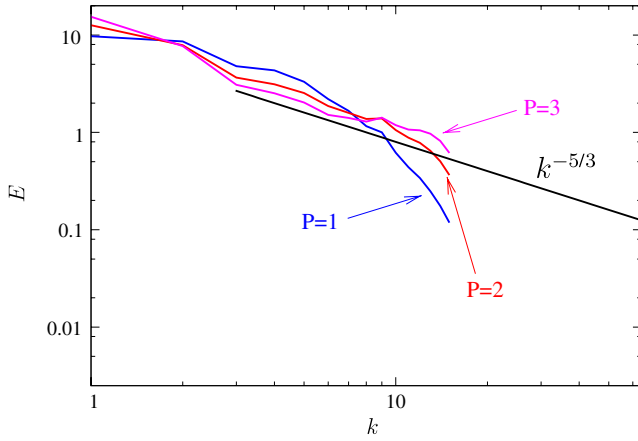
Fig. 14. Two-point third-order structure functions for  $h$ -refinement.  $Re_\lambda = \infty$ .

is about 165 for all cases, where  $\epsilon$  is the dissipation (see [58]). Once the simulation reaches equilibrium, the power input,  $P_{in}$ , is equal to the dissipation of the simulation. This result is in good agreement with the DNS data. Results are compared with the data provided by Moser, which is described in [52]. For  $Re_\lambda = \infty$  the viscosity is set to zero. In this case we compare with theoretical correlations (see [58]).

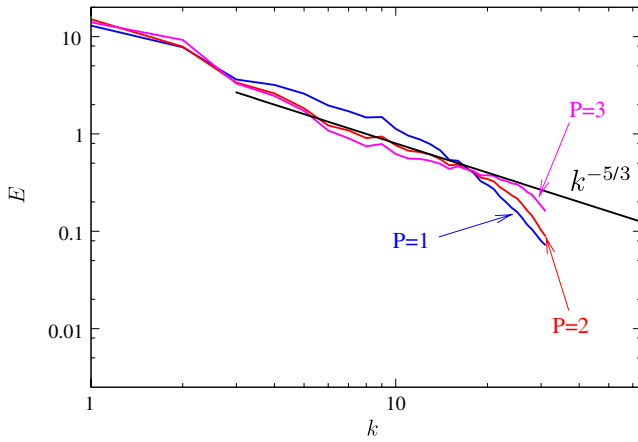
### 6.5. Simulation results

The quantities of interest are the energy spectrum and the two-point third-order structure function. The two-point third-order structure function is defined as

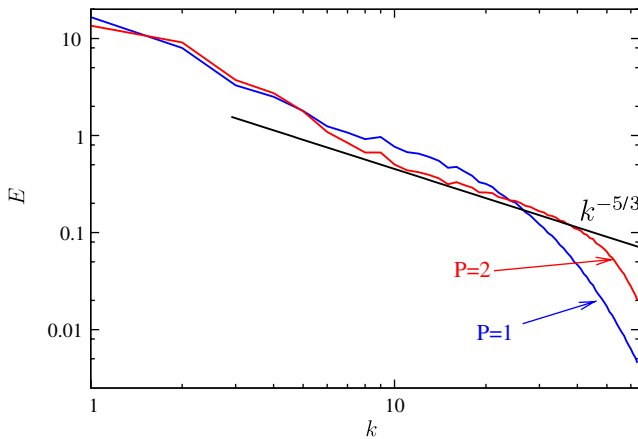
$$S_3(r) = \langle (\mathbf{u}(x+r) - \mathbf{u}(x))^3 \rangle, \quad (131)$$



(a) Meshes of  $32^3$  elements

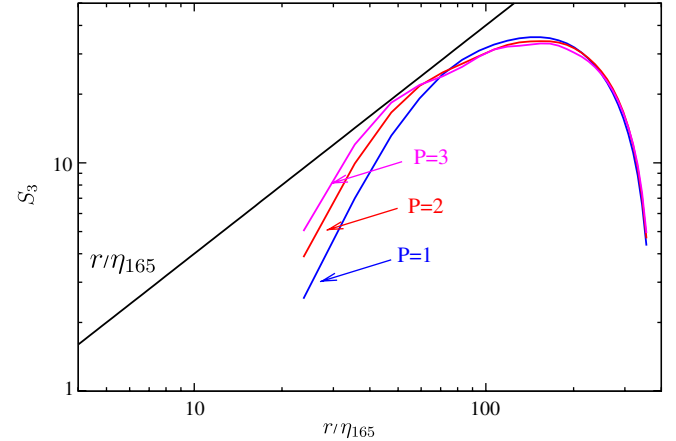


(b) Meshes of  $64^3$  elements

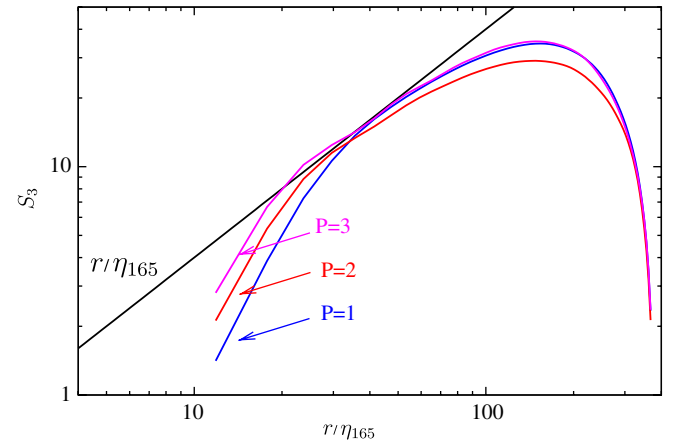


(c) Meshes of  $128^3$  elements

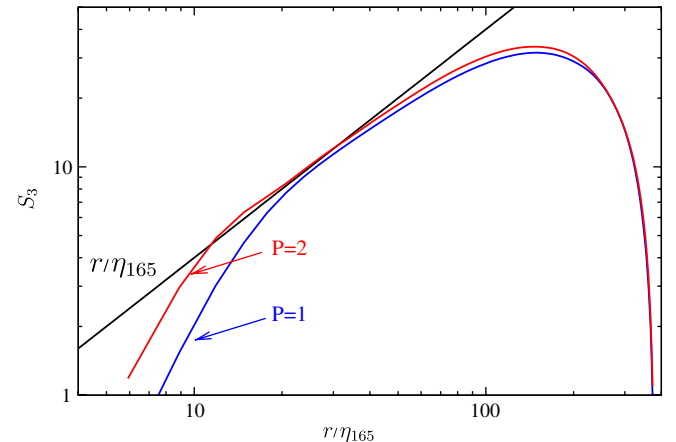
Fig. 15. Energy spectra for  $k$ -refinement.  $Re_\lambda = \infty$ .



(a) Meshes of  $32^3$  elements



(b) Meshes of  $64^3$  elements



(c) Meshes of  $128^3$  elements

Fig. 16. Two-point third-order structure functions for  $k$ -refinement.  $Re_\lambda = \infty$ .

where  $\langle \cdot \rangle$  implies ensemble average. In the inertial sub-range,  $S_3$  scales like  $r$  for fully-developed, locally isotropic turbulence (see [58, p. 204]). Due to the role played by  $S_3$  in the Karman–Howarth equation, an accurate representation of  $S_3$  implies an accurate description of the energy transfer in the inertial sub-range.

Data samples were collected for at least 20 eddy turnover times,  $T_{\text{ett}} = q^2/(2\epsilon)$ . Samples were separated by about  $0.4 T_{\text{ett}}$ . The spatial sampling is performed at knots and the mid-points between knots. For example, in the simulation of  $32^3$ , we sample on a  $64^3$  uniform mesh.

#### Remarks

- (1) We investigated the possibility that  $\rho_\infty$ , the parameter in the generalized- $\alpha$  method that controls its numerical high-frequency dissipation, affected results.

We ran cases with  $\rho_\infty = 1$  (no dissipation), 0.5 (our default value) and 0 (maximal dissipation). We found no discernible differences in the computed statistics. This may have been due to the very small time steps used in the calculations, typically of the order of 0.2 the advective Courant number, where the advective speed is defined as  $\sqrt{q}$ .

- (2) We note that it is important to precisely converge the nonlinear residual of the coarse-scale equations in every time step. We reduced the residual in each step to  $10^{-5}$  of its initial value. Failure to sufficiently converge the residual leads to spurious dissipation in our experience.

The data are presented in two complementary fashions. Figs. 6, 7, 13, and 14 illustrate  $h$ -refinement, whereas Figs. 8, 9, 15 and 16 illustrate  $k$ -refinement (see [30]).

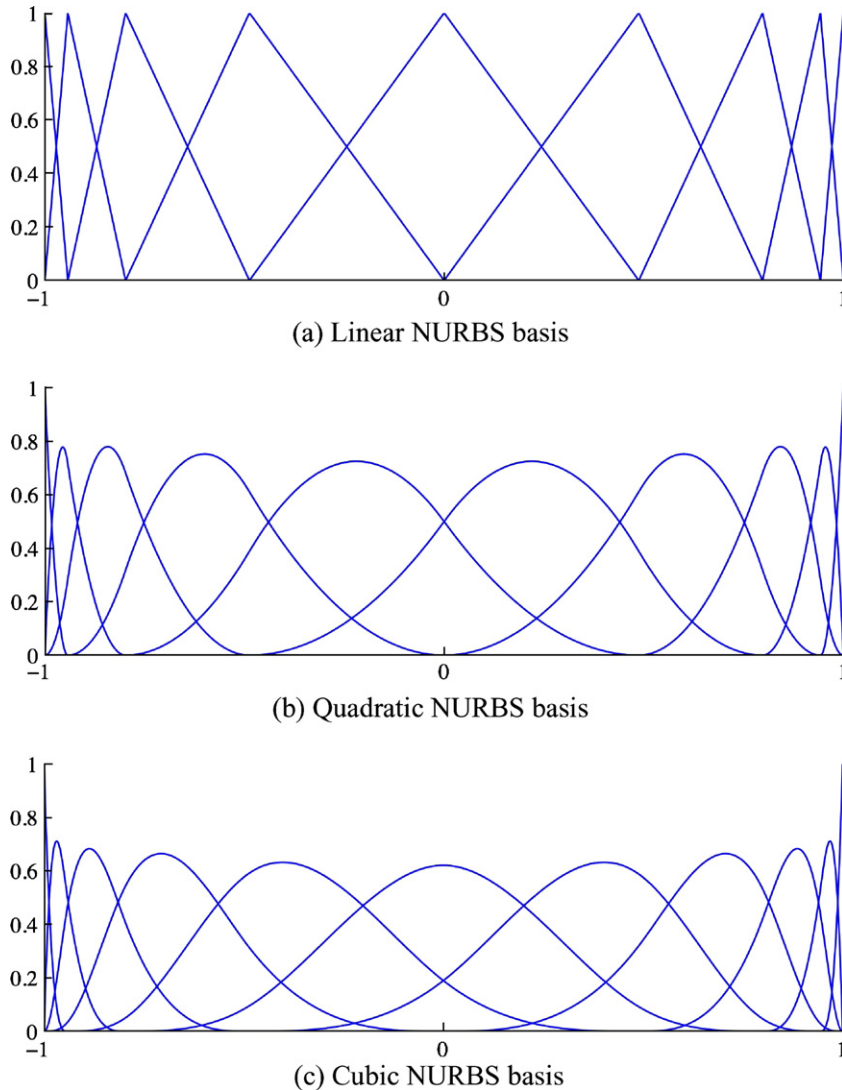


Fig. 17. Illustration of the wall-normal discretization for the turbulent channel flow problem. Meshes are graded towards the ends of the interval in order to better resolve boundary layers. Note that, due to the open knot vector construction (see [30] for details), the first and last basis functions are interpolatory at the endpoints of the domain, which facilitates strong imposition of no-slip Dirichlet boundary conditions.



### 6.5.1. $Re_\tau = 165$

Fig. 6 shows that the energy spectrum has no energy pile up at high-wave numbers for all orders and numbers of degrees-of-freedom. In fact, all energy spectra are in good agreement with the DNS, even for coarse meshes. In Fig. 6, we observe that about half the wave numbers for linear basis functions are in close agreement with the DNS spectrum, while this ratio significantly improves for higher-order basis functions, becoming almost 100% for the cubic case at  $64^3$ . In Fig. 7, the third-order structure function is plotted against the non-dimensional distance

$r/\eta$ , where  $\eta$  is the Kolmogorov dissipative scale [58], defined as

$$\eta = \left( \frac{v^3}{\epsilon} \right)^{1/4}. \quad (132)$$

As  $r/\eta$  increases the velocity field should decorrelate, which is observed in our calculations and the DNS. However, the forcing utilized in the DNS is somewhat different than that utilized here. In the DNS, the forcing occurs within a sphere of radius 3 in spectral space, whereas in our calculations, the

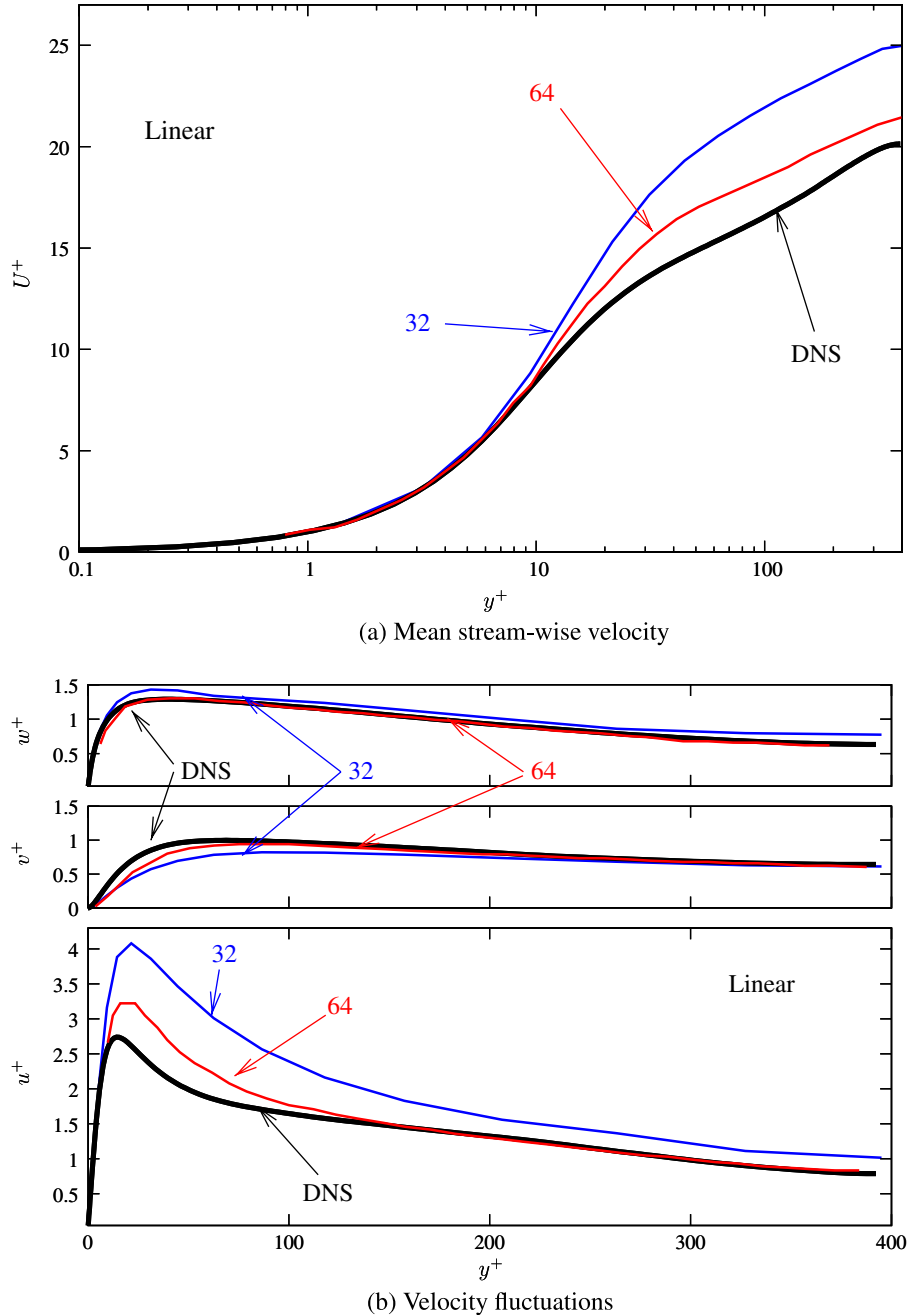


Fig. 18. Turbulent channel flow at  $Re_\tau = 395$  computed using linear NURBS:  $h$ -refinement interpretation of results.

forcing was performed within a box of half-edge-length 3. Thus, the small discrepancies between our results and the DNS for large values of  $r/\eta$  are to be expected. Fig. 7 shows that for each order, improved agreement with DNS is attained by increasing the number of degrees-of-freedom. Figs. 8 and 9 show that order elevation improves the agreement with DNS. It is particularly evident from these figures, that the most significant payoff is achieved when increasing the order from linear to quadratic.

Figs. 10 and 11 show snapshots of vorticity isosurfaces and velocity streamlines computed on a  $128^3$  mesh of

quadratic NURBS. Fig. 12 shows a detail of a single vortex tube computed on a mesh of  $64^3$  cubic NURBS. The visualizations are performed using techniques from Johnson et al. [46,47].

#### 6.5.2. $Re_\lambda = \infty$

The  $Re_\lambda = \infty$  case (i.e.,  $\nu = 0$ ) is felt to be relevant to practical engineering situations in which the resolution is inadequate to represent the physical flow features, even with an LES approach (see [54]). What one hopes to see in an LES is a distinct branch of the energy spectrum

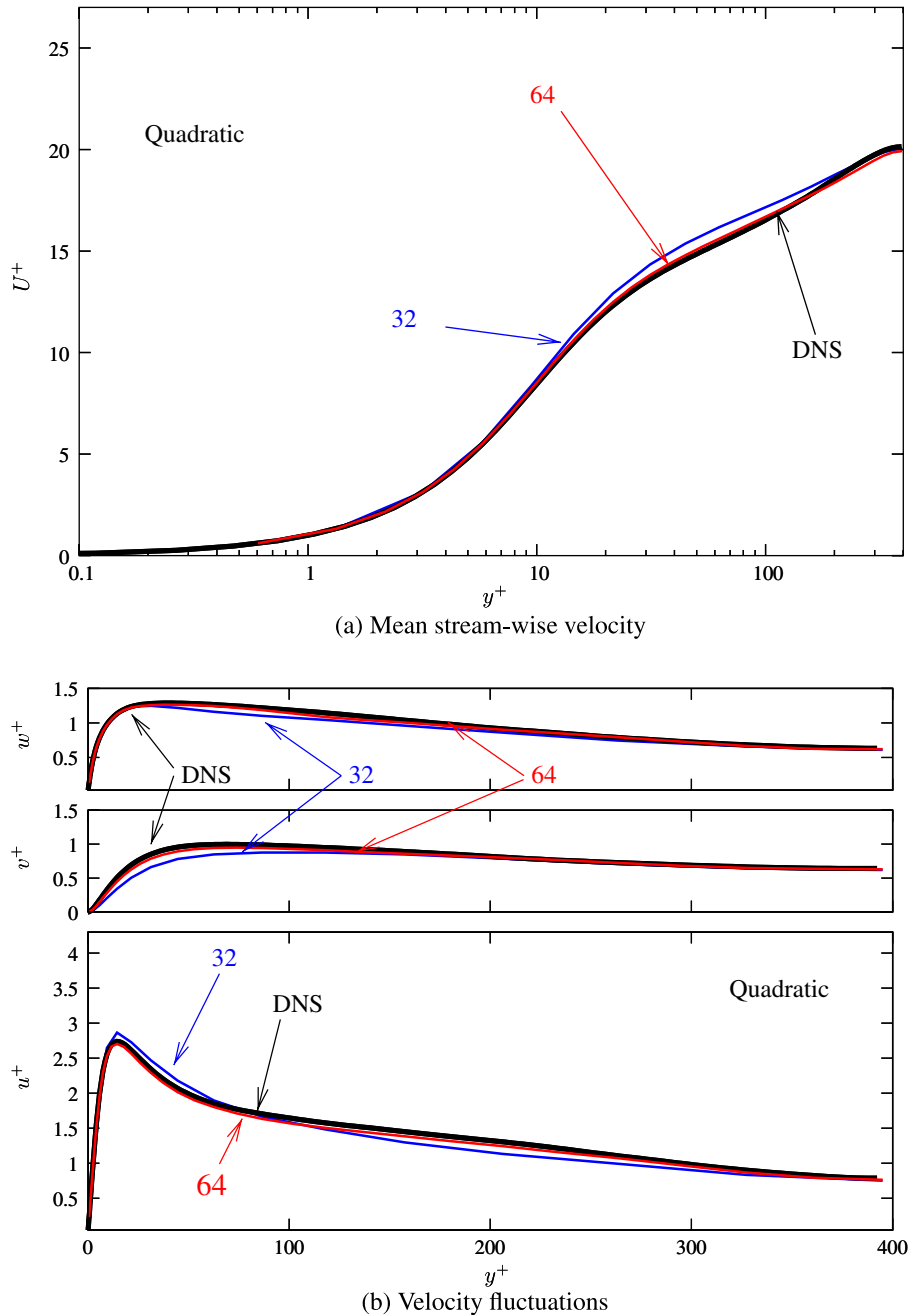


Fig. 19. Turbulent channel flow at  $Re_\tau = 395$  computed using quadratic NURBS:  $h$ -refinement interpretation of results.

corresponding to the inertial range, without an energy pile-up at the cut-off wave number. Likewise, there is a theoretical inertial-range scaling for the two-point third-order structure function. In the present circumstances, the forcing occurs for  $|k_i| < k_f = 3$ ,  $i = 1, 2, 3$ , but beyond this value we expect to see a transition to an inertial range, at least for a sufficiently fine mesh.

From Figs. 13 and 15, we observe that, for all orders and discretizations, no energy pile up occurs in the highest wave numbers in the computed energy spectra. Beyond the regime of forcing, the expected Kolmogorov  $k^{-5/3}$  spectrum is clearly discernible. It is interesting to observe from Fig. 13 that the tail off of the spectrum at high wave num-

bers diminishes as the order of approximation is increased. To facilitate the comparison of Figs. 14 and 16 with Figs. 7 and 9, respectively, we employ the same scaling in Figs. 14 and 16 as the one we used in Figs. 7 and 9. In Figs. 14 and 16 we emphasize this point by the notation  $\eta_{165}$ . Again, the development of the inertial range is evident.

## 7. Turbulent channel flow

Our next numerical example is an equilibrium turbulent channel flow at Reynolds number 395 based on the friction velocity and the channel half width. The computational domain is a rectangular box of size  $2\pi \times 2 \times 2/3\pi$  in the

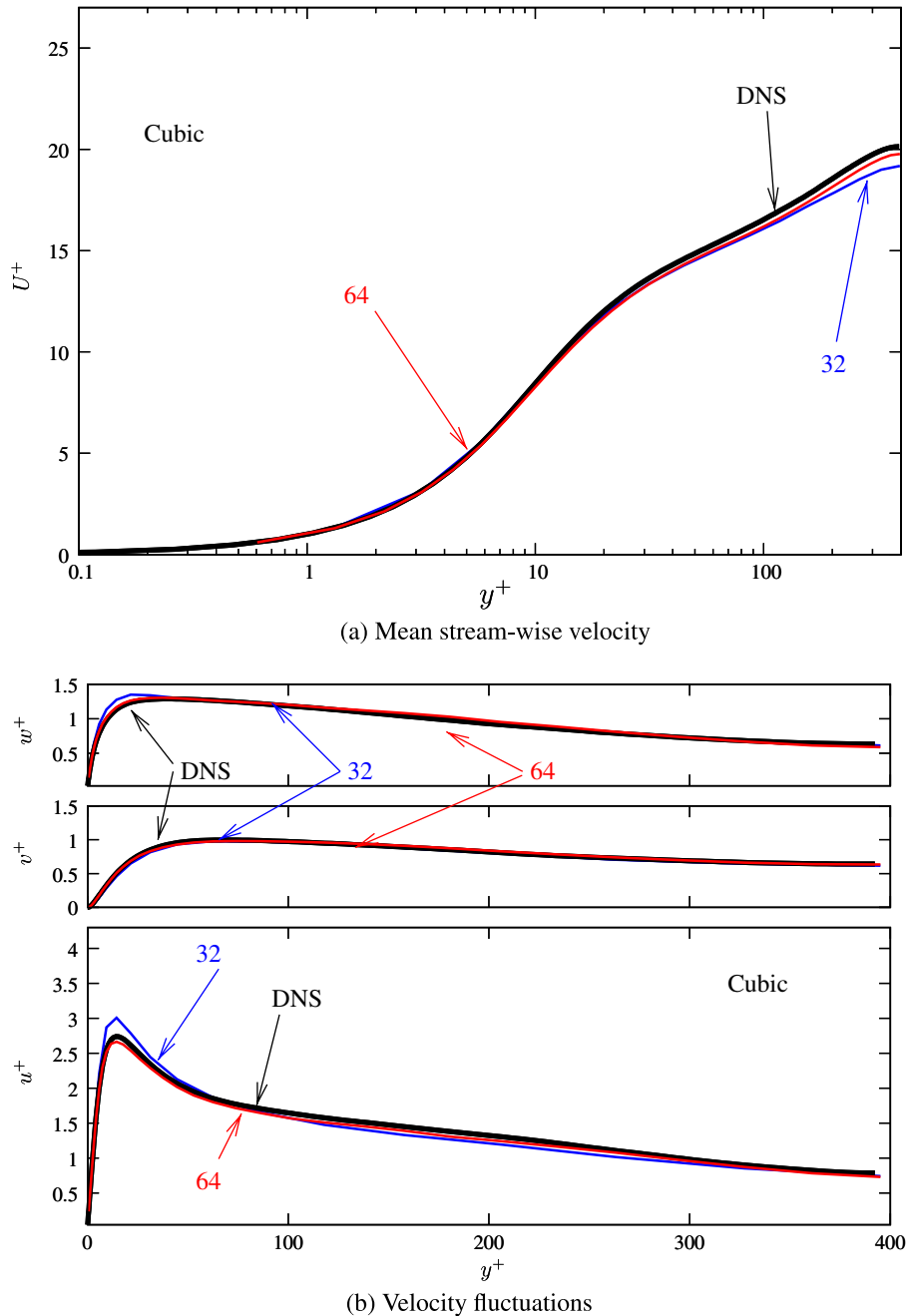


Fig. 20. Turbulent channel flow at  $Re_\tau = 395$  computed using cubic NURBS:  $h$ -refinement interpretation of results.

stream-wise, wall-normal, and span-wise directions, respectively. A no-slip Dirichlet boundary condition is set at the wall ( $y = \pm 1$ ), while the stream-wise and the span-wise directions are assigned periodic boundary conditions. The no-slip condition is imposed strongly, that is, velocity degrees of freedom are explicitly set to zero at the wall. Alternatively, one may enforce the no-slip conditions weakly by augmenting the discrete formulation with terms that enforce Dirichlet conditions as Euler–Lagrange conditions (see [6,7]). Although the weak boundary condition approach was shown to be superior to the strong imposition, we did not employ it in the computations reported

in this paper. The manner of specifying periodic conditions is identical to the case of homogeneous isotropic turbulence. The flow is driven by a constant pressure gradient,  $f_x$ , acting in the stream-wise direction. The values of the kinematic viscosity  $\nu$  and the forcing  $f_x$  are set to  $1.47200 \times 10^{-4}$  and  $3.372040 \times 10^{-3}$ , respectively.

The computations were performed on meshes of  $32^3$  and  $64^3$  elements. For both meshes we employ  $C^0$ -continuous linear,  $C^1$ -continuous quadratic, and  $C^2$ -continuous cubic NURBS. For all orders, in the stream-wise and the span-wise directions the number of basis functions is equal to the number of elements in these directions. On the other

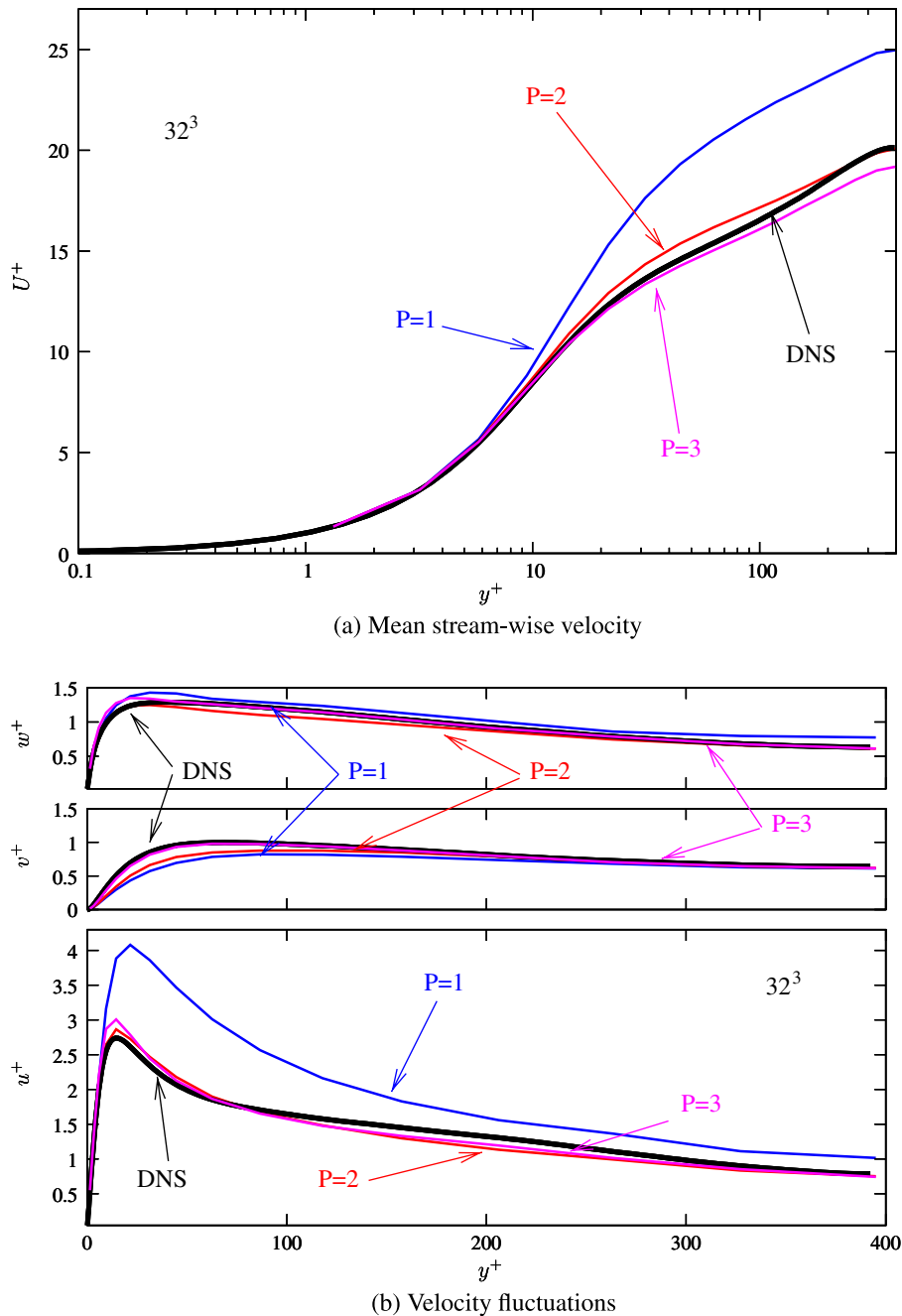


Fig. 21. Turbulent channel flow at  $Re_\tau = 395$  computed on a mesh of  $32^3$  elements:  $k$ -refinement interpretation of results.



hand, due to the open knot vector construction (see Fig. 17), the number of basis functions in the wall-normal direction is  $n_y = n_{el} + p$ , where  $n_{el}$  is the number of elements in this direction and  $p$  is the polynomial order.

Numerical results for this test case are reported in the form of statistics of the mean stream-wise velocity and root-mean-square velocity fluctuations. Statistics are obtained by sampling the solution fields at the mesh knots and averaging in the stream-wise and span-wise directions as well as in time. Comparison of the statistical quantities of interest with the DNS data of Moser et al. [55] is made

in order to assess the accuracy of the proposed turbulence modeling methodology. All results are presented in non-dimensional wall units. Both  $h$ -refinement (Figs. 18–20) and  $k$ -refinement (Figs. 21 and 22) viewpoints are presented.

Refining the mesh by a factor of two in each direction results in a much more accurate solution for linear elements, which is evident from Fig. 18. Note from Figs. 19 and 20 that for a mesh of  $64^3$  elements both quadratic and cubic solutions are almost identical to the DNS result. Also note that the  $32^3$  mesh solutions for quadratic and

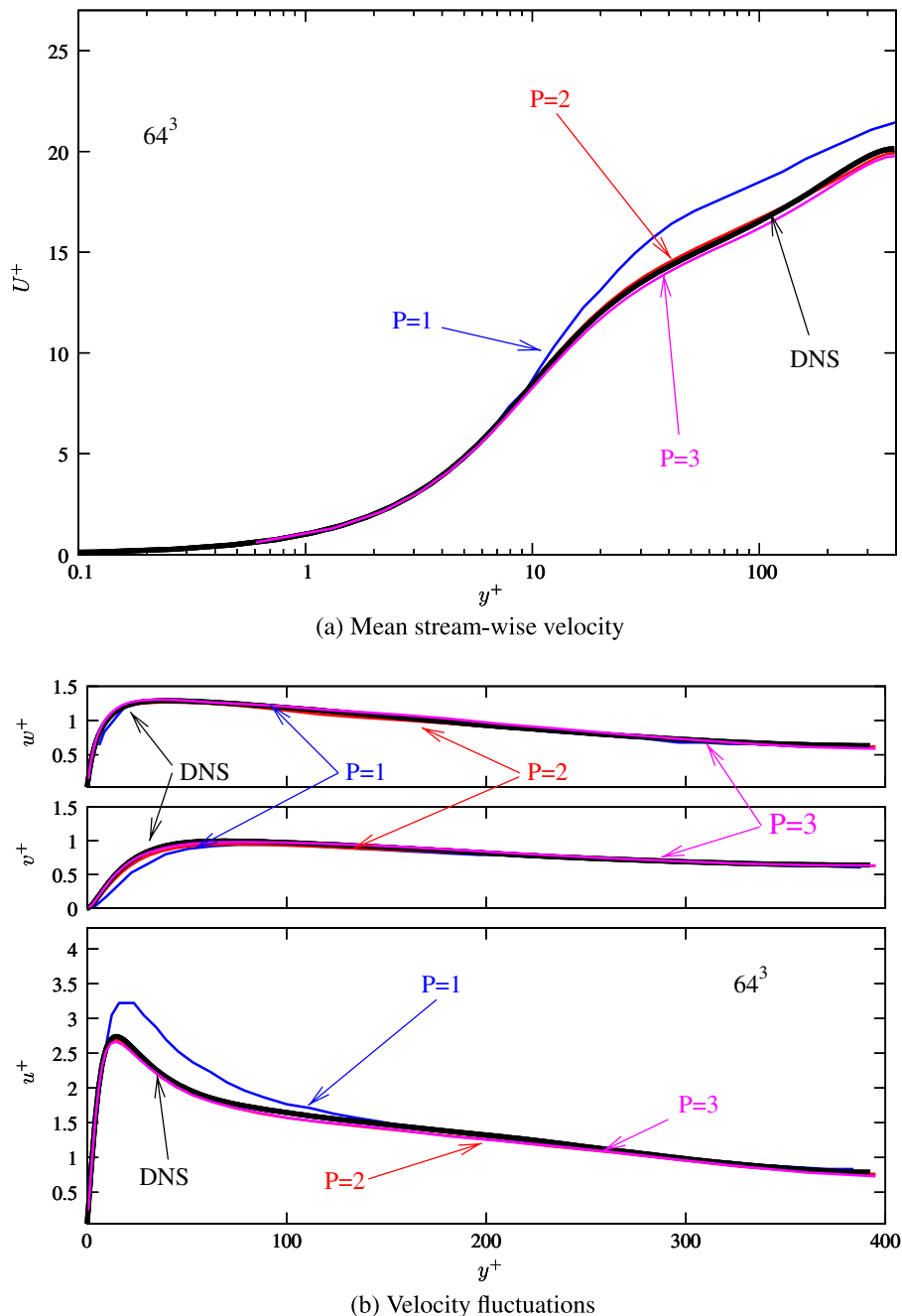


Fig. 22. Turbulent channel flow at  $Re_\tau = 395$  computed on a mesh of  $64^3$  elements:  $k$ -refinement interpretation of results.

cubic NURBS are significantly more accurate than the  $64^3$  mesh solution for linear elements (compare Figs. 19 and 20 with 18).

In Fig. 21, on the  $32^3$  mesh, linear elements show a significant over-prediction of the mean stream-wise velocity in the log layer. Fluctuations in the stream-wise velocity are also over-predicted as compared to the DNS result. On the same mesh, quadratic and cubic NURBS show good accuracy in both mean and fluctuating quantities. Notice the significant increase in accuracy when going from linear to quadratic NURBS, while increasing the order of approximation to cubic yields results that are not much different than for quadratic NURBS. The same trends are evident in Fig. 22. However, here it is clear that the quadratic and cubic results are virtually identical to the DNS results.

The results for  $32^3$  quadratic and cubic NURBS are even better than high-fidelity spectral Galerkin LES results presented in [36,27]. We note though that the formulation utilized in [36,27] employed a fine-scale eddy viscosity model and is quite different from the one used here.

Fig. 23 shows isosurfaces of stream-wise velocity, velocity streamlines, and a series of snapshots of particles released at the channel inflow and set in motion to follow the streamlines in the boundary layer.

## 8. Conclusions

We presented a general variational multiscale theory suitable for LES-type turbulence modeling. The theory is derived directly from the incompressible Navier–Stokes equations and does not involve any *ad hoc* mechanisms. In particular, it entirely avoids use of eddy viscosities. We feel that this theory of turbulence modeling is more fundamental and logically consistent than ones derived heretofore and it has significant potential in practical engineering calculations. One of the primary reasons we feel this way is that NURBS, in the context of the isogeometric concept [30,19,5]), are capable of precisely modeling complex geometric configurations. This feature was not exploited herein where we focused on the physics of turbulence in simple geometries, but the code we utilized is the same one we have successfully employed in a variety of complex laminar and turbulent, fluid and fluid–structure interaction computations (see [3,4,77]). We might also mention that the turbulence modeling aspects remain *unaltered* when we consider laminar flows. In this sense, our methodology may be viewed as an approach for solving the incompressible Navier–Stokes equations, whether the flow under consideration is laminar or turbulent, or both (see [14]). We

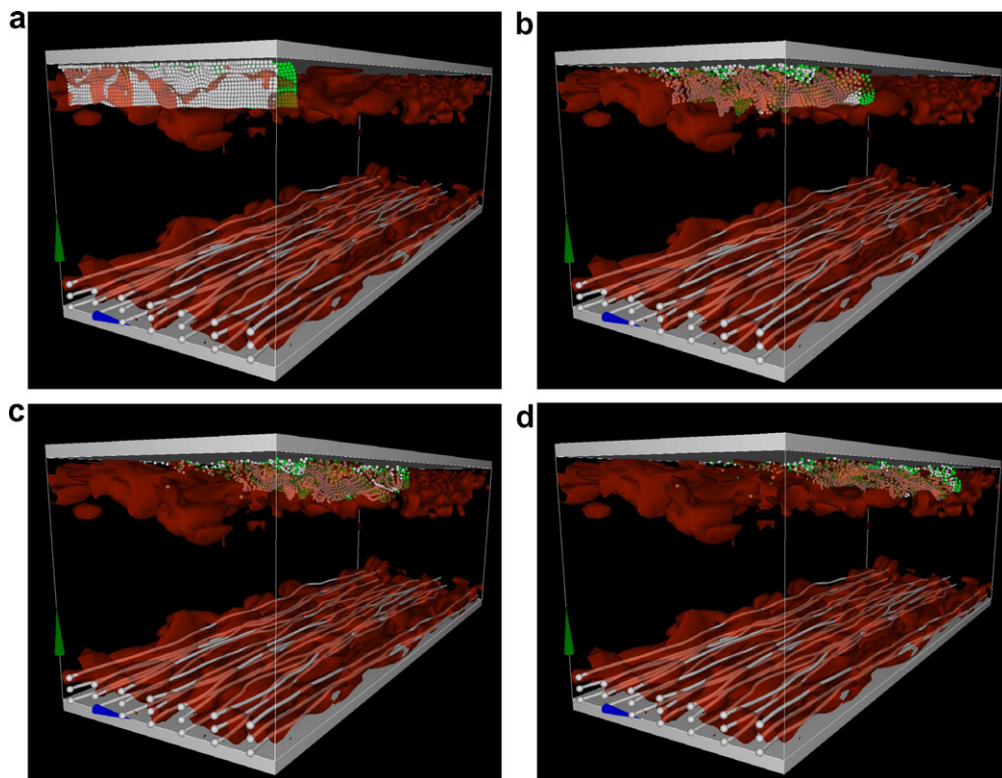


Fig. 23. Turbulent channel flow at  $Re_\tau = 395$ . Flow streamlines and isosurfaces of stream-wise velocity. Two parallel planes of particles, colored white and green, are released at the channel inflow close to the wall (see (a)), and are set in motion to follow the streamlines. Snapshots of the particle field are shown as particles travel down the length of the channel (see (b)–(d)). One can see the formation of the boundary layer as the particles released closer to the wall travel at slower speeds compared to the ones released in the outer layer. Also note that the particles initially released on different planes are mixed together as they approach the outflow, revealing the presence of faster and slower streaks in the boundary layer. Solution on the mesh of  $32^3$  quadratic NURBS was used for this visualization.

also believe that this aspect separates our theory of turbulence modeling from predecessors.

The calculations we performed of forced homogeneous isotropic turbulence and turbulent channel flows demonstrated that even the simplest residual-based modeling of fine scales by asymptotic scaling arguments is capable of giving very good results, at least in the LES context. Nevertheless, we feel that this is an area in which it is almost inevitable that there will be significant improvement. Research is under way to develop better approximations to fine-scale behavior. We may mention the important work of Codina et al. [16] and work that we also have in progress and hope to report on in the near future.

We wish to emphasize the importance of the fine-scale modeling problem. It represents the only open issue within our theory of turbulence modeling because the coarse-scale equation, the one we solve numerically, is exact in the sense that the dependence on the fine scales is exact, that is, there is no approximation until the fine scales are substituted into it. For this reason, we feel significant effort should be devoted to studying the fine-scale problem, both theoretically and computationally. One area that deserves attention is directly addressing nonlinearities in the fine-scale approximation rather than dealing with them through perturbation and linearization procedures. In the context of scaling arguments, an initial investigation was performed in [14].

The role of NURBS should also not be underestimated, at least in comparison with classical finite elements. We showed through dispersion analysis of one-dimensional model problems that NURBS gave significantly better approximations of advective and diffusive behavior. This was particularly dramatic in the high-wave number portion of the spectrum in diffusive processes. We conjectured that this was an advantage in LES turbulence modeling due to the participation of all resolved wave numbers in a numerical calculation. In a companion study we performed a comparison of NURBS and classical finite elements on turbulent channel flows, and the results confirmed our conjecture (see [1]).

The gold standard in turbulence has always been spectral methodology. NURBS give near-spectral approximations yet are applicable to the most complex geometries through the isogeometric concept. Although classical finite elements are capable of approximating complex geometries, they are not capable of high-precision geometric modeling because curved geometries are modeled with piece-wise polynomial facets. On the other hand, NURBS are undoubtedly the most widely used technology for modeling curved surfaces in geometric design, and even quadratic NURBS are capable of exactly representing all conic sections (i.e., circles, cylinders, spheres, ellipsoids, etc.), which are ubiquitous in engineering design. Furthermore, it is not yet fully appreciated how poorly classical higher-order finite elements approximate higher wave numbers. We believe the divergent behavior of the approximation with increasing order is a deficiency in turbulence, and, we conjecture, in other situations as well. On the contrary,

the good behavior of NURBS over the entire wave-number spectrum, combined with their superiority in geometric representation, seem to make them an ideal general purpose technology for turbulent flow simulation of complex engineering designs.

An issue that needs to be investigated is the relationship, if any, with compact finite differences (see [53]). If a relationship can be established, it may be very beneficial in generalizing compact finite differences to complex geometries and in suggesting fast computer implementations of NURBS approximations.

Given that the scale separation in the present methodology is performed with respect to the coarse-scale space actually used in the numerical computations, that is, the resolved scales, and that the fine-scale approximation is rendered well defined by a projector used to make precise the direct sum decomposition into coarse and fine scales, it is impossible to entirely separate modeling and numerical concepts. We accept this as a fact associated with correct LES-type modeling concepts, not a shortcoming. However, other modeling concepts are certainly possible within the variational multiscale framework, including ones, which are not directly associated with numerical approximation, such as is the case of RANS.

We also believe that our theory is more coherent mathematically than previous formulations and that it may be possible to use it as a basis of a statistical analysis of convergence and approximation. This would represent a very significant step forward for the theory of turbulence modeling, but, admittedly, a very difficult one to achieve. Nevertheless, we feel a door has been opened for the construction of a mathematical theory.

We found quadratic NURBS to give very significant accuracy advantages over linear elements. This, combined with their geometric approximation superiority, and small computational overhead compared with linear elements (about 50% in our computations), suggests to us that they should be considered a preferred practical tool for engineering computations. Cubics, on the other hand, increased cost considerably (by about 100% compared to quadratics), largely due to cache overflow in element calculations. These remarks need to be qualified by the fact that our implementation of higher-order elements is not yet optimized in any way. We hope to significantly improve efficiency in future work.

In summary, we feel a new paradigm for turbulence modeling has been established. Initial results seem to indicate its accuracy per degree of freedom is superior or, at the least, equal to any procedure proposed heretofore. Its generality and geometric flexibility also suggest it may provide a more powerful approach to turbulence calculations than previously existed.

## Acknowledgements

We wish to express our appreciation for support provided by the Office of Naval Research under Contract No. N00014-03-0263, Dr. Luise Couchman, contract

monitor, and Sandia National Laboratories under Contract No. 114166. We also wish to thank R.D. Moser for guidance and many helpful suggestions, his students, Amitabh Bhattacharya and Paolo Zandonade, for their help with the isotropic turbulence DNS data, Greg Johnson and Karla Vega of Texas Advanced Computing Center [71] for the visualizations in Figs. 10–12 and 23. We also would like to thank TACC for granting us access to their computing facilities. Y. Bazilevs was partially supported by the J.T. Oden ICES Postdoctoral Fellowship at the Institute for Computational Engineering and Sciences (ICES). A. Reali was partially supported by the J.T. Oden Faculty Fellowship Research Program at the ICES. G. Scovazzi was partially supported under Sandia Laboratories LDRD “A Mathematical Framework for Multiscale Science and Engineering: The Variational Multiscale Method and Interscale Transfer Operators”, contract monitor Dr. S. Scott Collis. This support is gratefully acknowledged.

## References

- [1] I. Akkerman, Y. Bazilevs, V.M. Calo, T.J.R. Hughes, S. Hulshoff, The role of continuity in residual-based variational multiscale modeling of turbulence. *Comput. Mech.*, 2007, doi: [doi:10.1007/s00466-007-0193-7](https://doi.org/10.1007/s00466-007-0193-7).
- [2] G.I. Barenblatt, *Similarity, Self-similarity, and Intermediate Asymptotics*, Cambridge University Press, 1996.
- [3] Y. Bazilevs, *Isogeometric Analysis of Turbulence and Fluid–Structure Interaction*, PhD Thesis, ICES, UT Austin, 2006.
- [4] Y. Bazilevs, V.M. Calo, Y. Zhang, T.J.R. Hughes, Isogeometric fluid–structure interaction analysis with applications to arterial blood flow, *Comput. Mech.* 38 (2006) 310–322.
- [5] Y. Bazilevs, L. Beirão da Veiga, J.A. Cottrell, T.J.R. Hughes, G. Sangalli, Isogeometric analysis: approximation, stability and error estimates for h-refined meshes, *Math. Mod. Methods Appl. Sci.* 16 (2006) 1031–1090.
- [6] Y. Bazilevs, T.J.R. Hughes, Weak imposition of Dirichlet boundary conditions in fluid mechanics, *Comp. Fluids* 36 (2007) 12–26.
- [7] Y. Bazilevs, C. Michler, V.M. Calo, T.J.R. Hughes, Weak Dirichlet boundary conditions for wall-bounded turbulent flows, *Comp. Methods Appl. Mech. Engrg.*, in press, 2007, doi: [doi:10.1016/j.cma.2007.06.026](https://doi.org/10.1016/j.cma.2007.06.026).
- [8] M. Behr, D. Hastreiter, S. Mittal, T.E. Tezduyar, Incompressible flow past a circular cylinder: dependence of the computed flow field on the location of the lateral boundaries, *Comp. Methods Appl. Mech. Engrg.* 123 (1996) 309–316.
- [9] P.B. Bochev, T.J.R. Hughes, G. Scovazzi, *A Multiscale Discontinuous Galerkin Method*, Springer Lecture Notes in Computer Science, vol. 3743, Springer, 2006.
- [10] F. Brezzi, L.P. Franca, T.J.R. Hughes, A. Russo,  $b = \int g$ , *Comp. Methods Appl. Mech. Engrg.* 145 (1997) 329–339.
- [11] L. Brillouin, *Wave Propagation in Periodic Structures*, Dover Publications Inc., 1953.
- [12] A.N. Brooks, T.J.R. Hughes, Streamline upwind/Petrov–Galerkin formulations for convection dominated flows with particular emphasis on the incompressible Navier–Stokes equations, *Comp. Methods Appl. Mech. Engrg.* 32 (1982) 199–259.
- [13] A. Buffa, T.J.R. Hughes, G. Sangalli, Analysis of the multiscale discontinuous Galerkin method for convection–diffusion problems, *SIAM J. Numer. Anal.* 44 (4) (2006) 1420–1440.
- [14] V.M. Calo, *Residual-based Multiscale Turbulence Modeling: Finite Volume Simulation of Bypass Transition*, PhD Thesis, Department of Civil and Environmental Engineering, Stanford University, 2004.
- [15] J. Chung, G.M. Hulbert, A time integration algorithm for structural dynamics with improved numerical dissipation: The generalized- $\alpha$  method, *J. Appl. Mech.* 60 (1993) 371–375.
- [16] R. Codina, J. Principe, O. Guasch, S. Badia, Time dependent subscales in the stabilized finite element approximation of incompressible flow problems, *Comp. Methods Appl. Mech. Engrg.* 196 (2007) 2413–2430.
- [17] E. Cohen, R. Riesenfeld, G. Elber, *Geometric Modeling with Splines. An Introduction*, A.K. Peters Ltd., Wellesley, MA, 2001.
- [18] S.S. Collis, *Multiscale Methods for Turbulence Simulation and Control*, Technical Report 034, MEMS, Rice University, 2002.
- [19] J.A. Cottrell, A. Reali, Y. Bazilevs, T.J.R. Hughes, Isogeometric analysis of structural vibrations, *Comp. Methods Appl. Mech. Engrg.* 195 (2006) 5257–5297.
- [20] C. Farhat, B. Koobus, Finite volume discretization on unstructured meshes of the multiscale formulation of large eddy simulations, in: F.G. Rammerstorfer, H.A. Mang, J. Eberhardsteiner (Eds.), *Proceedings of the Fifth World Congress on Computational Mechanics (WCCM V)*, Vienna University of Technology, Austria, July 7–12, 2002.
- [21] G.E. Farin, *NURBS Curves and Surfaces: From Projective Geometry to Practical Use*, A.K. Peters, Ltd., Natick, MA, 1995.
- [22] V. Gravemeier, The variational multiscale method for laminar and turbulent flow, *Arch. Comput. Methods Engrg. – State of the Art Rev.* 13 (2006) 249–324.
- [23] P.M. Gresho, R.L. Sani, *Incompressible Flow and the Finite Element Method*, Wiley, New York, NY, 1998.
- [24] G. Hauke, M.H. Doweidar, M. Miana, The multiscale approach to error estimation and adaptivity, *Comp. Methods Appl. Mech. Engrg.* 195 (2006) 1573–1593.
- [25] G. Hauke, M.H. Doweidar, M. Miana, Proper intrinsic scales for a posteriori multiscale error estimation, *Comp. Methods Appl. Mech. Engrg.* 195 (2006) 3983–4001.
- [26] J. Hoffman, C. Johnson, Stability of the dual Navier–Stokes equations and efficient computation of mean output in turbulent flow using adaptive DNS/LES, *Comp. Methods Appl. Mech. Engrg.* 195 (2006) 1709–1721.
- [27] J. Holmen, T.J.R. Hughes, A.A. Oberai, G.N. Wells, Sensitivity of the scale partition for variational multiscale LES of channel flow, *Phys. Fluids* 16 (3) (2004) 824–827.
- [28] T.J.R. Hughes, Multiscale phenomena: Green’s functions, the Dirichlet-to-Neumann formulation, subgrid scale models, bubbles and the origins of stabilized methods, *Comp. Methods Appl. Mech. Engrg.* 127 (1995) 387–401.
- [29] T.J.R. Hughes, *The Finite Element Method: Linear Static and Dynamic Finite Element Analysis*, Dover Publications, Mineola, NY, 2000.
- [30] T.J.R. Hughes, J.A. Cottrell, Y. Bazilevs, Isogeometric analysis: CAD, finite elements, NURBS, exact geometry, and mesh refinement, *Comp. Methods Appl. Mech. Engrg.* 194 (2005) 4135–4195.
- [31] T.J.R. Hughes, G. Feijóo, L. Mazzei, J.B. Quincy, The variational multiscale method—Aparadigm for computational mechanics, *Comp. Methods Appl. Mech. Engrg.* 166 (1998) 3–24.
- [32] T.J.R. Hughes, M. Mallet, A new finite element formulation for fluid dynamics: III. The generalized streamline operator for multidimensional advective–diffusive systems, *Comp. Methods Appl. Mech. Engrg.* 58 (1986) 305–328.
- [33] T.J.R. Hughes, L. Mazzei, K.E. Jansen, Large-eddy simulation and the variational multiscale method, *Comp. Vis. Sci.* 3 (2000) 47–59.
- [34] T.J.R. Hughes, L. Mazzei, A.A. Oberai, A.A. Wray, The multiscale formulation of large eddy simulation: decay of homogenous isotropic turbulence, *Phys. Fluids* 13 (2) (2001) 505–512.
- [35] T.J.R. Hughes, A.A. Oberai, Calculation of shear stresses in Fourier–Galerkin formulations of turbulent channel flows: projection, the Dirichlet filter and conservation, *J. Comput. Phys.* 188 (1) (2003) 281–295.
- [36] T.J.R. Hughes, A.A. Oberai, L. Mazzei, Large-eddy simulation of turbulent channel flows by the variational multiscale method, *Phys. Fluids* 13 (6) (2001) 1784–1799.



- [37] T.J.R. Hughes, G. Sangalli, Variational multiscale analysis: the fine-scale Green's function, projection, optimization, localization, and stabilized methods, *SIAM J. Numer. Anal.* 45 (2007) 539–557.
- [38] T.J.R. Hughes, G. Scovazzi, P.B. Bochev, A. Buffa, A multiscale discontinuous Galerkin method with the computational structure of a continuous Galerkin method, *Comp. Methods Appl. Mech. Engrg.* 195 (2006) 2761–2787.
- [39] T.J.R. Hughes, G. Scovazzi, L.P. Franca, Multiscale and stabilized methods, in: E. Stein, R. De Borst, T.J.R. Hughes (Eds.), *Encyclopedia of computational mechanics*, Computational Fluid Dynamics, vol. 3, Wiley, 2004 (Chapter 4).
- [40] T.J.R. Hughes, J. Stewart, A space-time formulation for multiscale phenomena, *J. Comput. Appl. Math.* 74 (1996) 217–229.
- [41] T.J.R. Hughes, G.N. Wells, A.A. Wray, Energy transfers and spectral eddy viscosity of homogeneous isotropic turbulence: comparison of dynamic Smagorinsky and multiscale models over a range of discretizations, *Phys. Fluids* 16 (2004) 4044–4052.
- [42] K.E. Jansen, S.S. Collis, C.H. Whiting, F. Shakib, A better consistency for low-order stabilized finite element methods, *Comp. Methods Appl. Mech. Engrg.* 174 (1999) 153–170.
- [43] K.E. Jansen, C.H. Whiting, G.M. Hulbert, A generalized- $\alpha$  method for integrating the filtered Navier–Stokes equations with a stabilized finite element method, *Comp. Methods Appl. Mech. Engrg.* 190 (1999) 305–319.
- [44] H. Jeanmart, G.S. Winckelmans, Comparison of recent dynamic subgrid-scale models in the case of the turbulent channel flow, in: *Proceedings of the Summer Program*, Center for Turbulence Research, Stanford University and NASA Ames, 2002.
- [45] C. Johnson, *Numerical Solution of Partial Differential Equations by the Finite Element Method*, Cambridge University Press, Sweden, 1987.
- [46] G.P. Johnson, V.M. Calo, K. Gaither, Interactive visualization and analysis of transitional flow, *IEEE Trans. Vis. Comp. Graphics*, submitted for publication.
- [47] G.P. Johnson, K. Gaither, V.M. Calo, Visualizing turbulent flow, in: *15th IEEE Visualization Conference*, Austin, TX, October 2004, p. 598.22.
- [48] B. Koobus, C. Farhat, A variational multiscale method for the large eddy simulation of compressible turbulent flows on unstructured meshes – application to vortex shedding, *Comp. Methods Appl. Mech. Engrg.* 193 (2004) 1367–1383.
- [49] A.G. Kravchenko, P. Moin, R. Moser, Zonal embedded grids for numerical simulation of wall-bounded turbulent flows, *J. Comput. Phys.* 127 (1996) 412–423.
- [50] A.G. Kravchenko, P. Moin, K. Shariff, B-spline method and zonal grids for simulation of complex turbulent flows, *J. Comput. Phys.* 151 (1999) 757–789.
- [51] W.Y. Kwok, R.D. Moser, J. Jiménez, A critical evaluation of the resolution properties of B-spline and compact finite difference methods, *J. Comput. Phys.* 174 (2001) 510–551.
- [52] J.A. Langford, R.D. Moser, Optimal LES formulations for isotropic turbulence, *J. Fluid Mech.* 398 (1999) 321–346.
- [53] S.K. Lele, Compact finite difference schemes with spectral-like resolution, *J. Comput. Phys.* 103 (1992) 16–42.
- [54] M. Lesieur, O. Métais, P. Comte, *Large Eddy Simulation of Turbulence*, Cambridge University Press, Cambridge, England, 2005.
- [55] R. Moser, J. Kim, R. Mansour, DNS of turbulent channel flow up to  $Re = 590$ , *Phys. Fluids* 11 (1999) 943–945.
- [56] A.A. Oberai, T.J.R. Hughes, The variational multiscale formulation of LES: channel flow at  $Re_\tau = 590$ , in: *40th AIAA Ann. Mtg.*, Reno, NV, 2002, AIAA 2002-1056.
- [57] L. Piegl, W. Tiller, *The NURBS Book* (Monographs in Visual Communication), 2nd ed., Springer-Verlag, New York, 1997.
- [58] S.B. Pope, *Turbulent Flows*, Cambridge University Press, Cambridge, 2000.
- [59] S. Ramakrishnan, S.S. Collis, Variational multiscale modeling for turbulence control, in: *AIAA 1st Flow Control Conference*, St. Louis, MO, June 2002, AIAA 2002-3280.
- [60] S. Ramakrishnan and S.S. Collis, Multiscale modeling for turbulence simulation in complex geometries, in: *40th AIAA Aerospace Sciences Meeting and Exhibit*, Reno, NV, Jan. 2004, AIAA 2004-0241.
- [61] S. Ramakrishnan, S.S. Collis, Turbulence control simulation using the variational multiscale method, *AIAA J.* 42 (4) (2004) 745–753.
- [62] S. Ramakrishnan, S.S. Collis, Partition selection in multiscale turbulence modeling, *Phys. Fluids* 18 (7) (2006).
- [63] D.F. Rogers, *An Introduction to NURBS with Historical Perspective*, Academic Press, San Diego, CA, 2001.
- [64] Y. Saad, M.H. Schultz, GMRES: a generalized minimal residual algorithm for solving nonsymmetric linear systems, *SIAM J. Sci. Stat. Comput.* 7 (1986) 856–869.
- [65] P. Sagaut, S. Deck, M. Terracol, *Multiscale and Multiresolution Approaches in Turbulence*, Imperial College Press, 2006.
- [66] G. Scovazzi, *Multiscale Methods in Science and Engineering*, PhD Thesis, Department of Mechanical Engineering, Stanford University. <http://www.cs.sandia.gov/gscovaz>, 2004.
- [67] F. Shakib, T.J.R. Hughes, Z. Johan, A new finite element formulation for computational fluid dynamics: X. The compressible Euler and Navier–Stokes equations, *Comp. Methods Appl. Mech. Engrg.* 89 (1991) 141–219.
- [68] K. Shariff, R.D. Moser, Two-dimensional mesh embedding for B-spline methods, *J. Comput. Phys.* 145 (1998) 471–488.
- [69] V. Sheffer, An inviscid flow with compact support in space-time, *J. Geom. Anal.* 3 (1993) 343–401.
- [70] J.C. Simo, T.J.R. Hughes, *Computational Inelasticity*, Springer-Verlag, New York, 1998.
- [71] Texas Advanced Computing Center (TACC). <http://www.tacc.utexas.edu>.
- [72] T.E. Tezduyar, Computation of moving boundaries and interfaces and stabilization parameters, *Int. J. Numer. Methods Fluids* 43 (2003) 555–575.
- [73] R. Vichnevetsky, J.B. Bowles, *Fourier Analysis of Numerical Approximations of Hyperbolic Equations*, Society for Industrial and Applied Mathematics, Philadelphia, 1982.
- [74] G.B. Whitham, *Linear and Nonlinear Waves*, John Wiley and Sons, New York, 1974.
- [75] C.H. Whiting, *Stabilized Finite Element Methods for Fluid Dynamics using a Hierarchical Basis*, PhD Thesis, Rensselaer Polytechnic Institute, September 1999.
- [76] C.H. Whiting, K.E. Jansen, A stabilized finite element method for the incompressible Navier–Stokes equations using a hierarchical basis, *Int. J. Numer. Methods Fluids* 35 (2001) 93–116.
- [77] Y. Zhang, Y. Bazilevs, S. Goswami, C. Bajaj, T.J.R. Hughes, Patient-specific vascular NURBS modeling for isogeometric analysis of blood flow, *Comp. Methods Appl. Mech. Engrg.* 196 (2007) 2943–2959.